People`s Democratic Republic of Algeria
Ministry of Higher Education and Scientific Research
University of Echahid Hamma Lakhdar - El Oued
Faculty of Technology
Department of Electrical Engineering

Dissertation

ACADEMIC MASTER

Domain: Science and Technology

Division: **Electrical Engineering**

Specialty: **Telecommunication Systems**

Presented by:

1. **Bounegab Abdelhak**
2. **Mehda Kinza**

Entitled:

Design and Optimization of Trilayer Perovskite Solar Cells Using SCAPS-1D Numerical Simulations

Dissertation Submitted in Partial Fulfillment of the Requirements for the Master Degree in **Telecommunication Systems**

Publicly defended in: **14/06/2026**

Board of Examiners:

Dr. Medjouri Abdelkader	**Chairman**
Dr. Tinedert Imad Eddine	**Supervisor**
Dr. Aourar Nabil	**Examiner**

Academic Year: 2025/2026

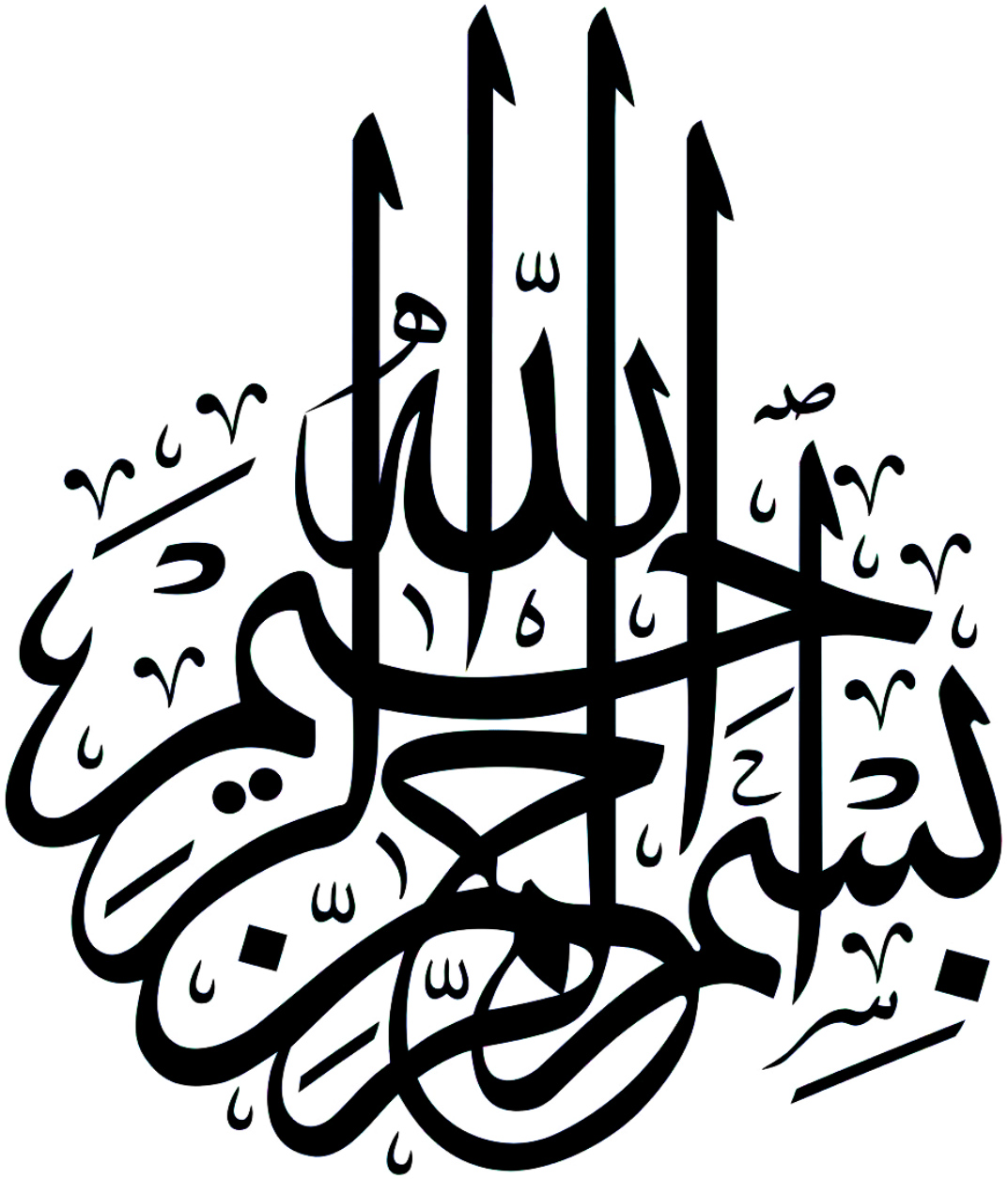
بسم الله الرحمن الرحيم

Acknowledgements

By the grace of God, this work has been successfully completed. All praise and thanks are due to Him for the strength, patience, and perseverance He bestowed upon me to finish this thesis.

We would like to express our sincere gratitude and appreciation to our supervisor, Dr. Tinedert Imad Eddine for his continuous guidance, valuable advice, and unwavering support throughout the preparation of this work. His encouragement and insightful comments were instrumental in the completion of this thesis.

We would also like to extend our deepest thanks to all our professors for the knowledge, experience, and wisdom they generously shared with us throughout our academic journey.

Dedication

To my beloved father, may God have mercy on him, who has departed this world but whose memory remains in my heart.

To my dear mother, my source of support and inspiration.

To my family and loved ones.

I dedicate to you the fruits of this labor.

Abdelhak

Thank you all.

Dedication

To the soul of my pure father, may God have mercy on him

whose dream was to see me successful

And I ask God to make this work in the balance of His good deeds

To my dear mother, the symbol of giving and patience

whose prayers and support were my greatest support in every step

To my older brother, who took part of the responsibility after my father 's departure, and I had support and help

To my beloved brothers, from whom I draw love and strength

And to my honorable professors, who have illuminated the path of science and knowledge with their valuable guidance and advice

To you all, I dedicate the fruit of this humble effort, wishing it to be a source of pride and happiness for you

Kinza

ملخص

أصبح الانتقال نحو الخلايا الشمسية البيروفسكايتية الخالية من الرصاص ضرورياً بسبب المخاوف المرتبطة بسمية المواد المحتوية على الرصاص. وللتغلب على محدودية الامتصاص الطيفي للخلايا الشمسية البيروفسكايتية أحادية الطبقة، تقترح هذه الدراسة بنية ثلاثية الطبقات متدرجة فجوة الطاقة. تم إجراء محاكاة عددية باستخدام برنامج SCAPS-1D لدراسة وتحسين أداء الخلايا الشمسية البيروفسكايتية الخالية من الرصاص. في البداية، تم تحليل خلية شمسية مرجعية أحادية الطبقة ذات البنية $ITO/TiO_2/K_2LiAlI_6/CuI/Au$، حيث حققت كفاءة تحويل قدرها 21.79%، وهو متوافق بشكل كبير مع القيم المبلغ عنها في الأدبيات العلمية. لتعزيز أداء الخلية، تم إدخال طبقة ماصة ثانية قائمة على $RbGeBr_3$ ، لتشكيل بنية ثنائية الطبقات ($ITO/TiO_2/K_2LiAlI_6/RbGeBr_3/CuI/Au$)ورفع الكفاءة إلى 33.51%. بعد ذلك، تم إضافة طبقة ماصة ثالثة، $FA4GeSbCl_{12}$، لتشكيل جهاز ثلاثي الطبقات بالبنية $ITO/TiO_2/K_2LiAlI_6/RbGeBr_3/FA_4GeSbCl_{12}/CuI/Au$، محققاً كفاءة 35.75.%. تم دراسة عدة مواد لنقل الثقوب (HTL) بما في ذلك CFTS ، Cu_2O، $CuCrO_2$، CuI، CuO، NiO، Spiro-OMeTAD، P3CPenT، PEDOT:PSS، و .CuSCN تم تحديد يوديد النحاس الأحادي (CuI) كأفضل مادة ناقلة للثقوب نظراً لتوافقها الممتاز مع البنية المقترحة، محققة عامل تعبئة عالٍ قدره 86.74%. علاوة على ذلك، تم تحسين سمك وتركيز المستقبلات (acceptor concentration) لطبقات الامتصاص الثلاث بشكل منهجي. تم العثور على السمك الأمثل ل K_2LiAlI_6 ، $RbGeBr_3$، و $FA_4GeSbCl_{12}$ ليكون 100 نانومتر، 500 نانومتر، و 800 نانومتر على التوالي، بينما كان تركيز المستقبلات الأمثل 1×10^{17} سم$^{-3}$، 2×10^{13} سم$^{-3}$، و 1×10^{20} سم$^{-3}$ على التوالي. ونتيجة لذلك، تم تحقيق أداء كهروضوئي ممتاز للجهاز الثلاثي المُحسَّن، بكفاءة تحويل طاقة قدرها 40.88%، وجهد دائرة مفتوحة 1.37 فولت، وكثافة تيار دائرة قصر 33.47مل أمبير/سم²، وعامل تعبئة 88.67% تحت إضاءة AM1.5G عند درجة حرارة 300 كلفن. تؤكد هذه النتائج فعالية التصميم الثلاثي متدرج فجوة الطاقة وتسلط الضوء على الإمكانات الكبيرة للمواد البيروفسكايتية الخالية من الرصاص لتطوير أجهزة كهروضوئية عالية الكفاءة من الجيل التالي.

الكلمات المفتاحية: طبقات امتصاص ثلاثية، PSCs، SCAPS-1D، PCE ، التحسين، فجوة النطاق.

Abstract

The transition toward lead-free perovskite solar cells has become essential due to the toxicity concerns associated with lead-based materials. To overcome the limited spectral absorption of single-layer lead-free perovskite solar cells, this study proposes a trilayer graded-bandgap architecture. A numerical simulation was carried out using SCAPS-1D software to investigate and optimize the performance of lead-free perovskite solar cells. Initially, a reference single-layer solar cell with the structure ITO/TiO_2/K_2LiAlI_6/CuI/Au was analyzed, yielding a power conversion efficiency of 21.79%, which is in close agreement with values reported in the literature. To further enhance device performance, a second absorber layer based on $RbGeBr_3$ was introduced, resulting in a bilayer structure (ITO/TiO_2/K_2LiAlI_6/$RbGeBr_3$/CuI/Au) and increasing the efficiency to 33.51%. Subsequently, a third absorber layer, $FA_4GeSbCl_{12}$, was incorporated to form a trilayer device with the structure ITO/TiO_2/K_2LiAlI_6/$RbGeBr_3$/$FA_4GeSbCl_{12}$/CuI/Au, achieving an efficiency of 35.75%. Several hole transport layer (HTL) materials were investigated, including CFTS, Cu_2O, $CuCrO_2$, CuI, CuO, NiO, Spiro-OMeTAD, P3CPenT, PEDOT:PSS, and CuSCN. Copper(I) iodide (CuI) was identified as the most suitable HTL due to its superior compatibility with the proposed device, achieving a high fill factor of 86.74%. Furthermore, the thickness and acceptor concentration of the three absorber layers were systematically optimized. The optimum thicknesses were found to be 100 nm, 500 nm, and 800 nm for K_2LiAlI_6, $RbGeBr_3$, and $FA_4GeSbCl_{12}$, respectively, while the optimum acceptor concentrations were 10^{17} cm^{-3}, 2×10^{13} cm^{-3}, and 10^{20} cm^{-3}, respectively. As a result, excellent photovoltaic performance was achieved for the optimized trilayer device, with a power conversion efficiency of 40.88%, an open-circuit voltage of 1.37 V, a short-circuit current density of 33.47 mA/cm^2, and a fill factor of 88.67% under AM1.5G illumination at a temperature of 300 K. These findings confirm the effectiveness of the proposed graded-bandgap trilayer design and highlight the strong potential of lead-free perovskite materials for the development of high-efficiency next-generation photovoltaic devices.

Keywords: Trilayer Absorbers, PSCs, SCAPS-1D, PCE, Optimization, Bandgap.

Table of contents

List of figures

List of tables

List of abbreviations

AM1.5G	Air Mass 1.5 Global
SCAPS	Solar Cell Capacitance Simulator
PSCs	Perovskite Solar Cells
PCE	Performance Conversion efficiency
E_g	Band gap energy
FF	Fill factor
J_{sc}	Short-circuit current density
V_{oc}	Open-circuit voltage
QE	Quantum efficiency
χ_e	Electron affinity
μ_n	Electron mobility
μ_p	Hole mobility
N_c	Conduction band effective density of states
N_v	Valence band effective density of states
N_d	Donor Carrier concentration
N_a	Acceptor Carrier concentration
N_t	Defect Density
R_s	Series resistance
R_{sh}	Shunt resistance
CB	Conduction Band
VB	Valence Band
EHP	Electron hole pair
EF	Fermi energy
TCO	Transparent conduction oxide
t_m	Thickness
HTL	Hole transport layer
ETL	Electron transport layer
ITO	Indium Tin Oxide
TiO_2	Titanium dioxide
$RbGeBr_3$	Rubidium Germanium Bromide
$FA_4GeSbCl_{12}$	Formamidinium Germanium-Antimony halide
CuI	Copper(I) iodide (CuI)

General Introduction

General Introduction

The Solar energy represents one of the most abundant and sustainable renewable energy sources available to humanity. The conversion of sunlight into electricity through photovoltaic (PV) technology has emerged as a critical solution to address the growing global demand for clean, environmentally friendly energy while mitigating the adverse effects of fossil fuel consumption. Among various renewable energy technologies, photovoltaic solar cells have attracted considerable attention due to their reliability, scalability, and potential to meet future energy needs. The discovery of solar cells dates back to the 19th century, when French physicist Alexandre Edmond Becquerel observed that directing sunlight onto certain electrical cells generates an electric current, a phenomenon later known as the photovoltaic effect. Since then, solar cell technology has undergone continuous development, leading to the emergence of various cell types depending on the materials used in their fabrication, including crystalline silicon cells, thin-film cells, organic cells, and perovskite-based cells. In recent years, perovskite solar cells (PSCs) have emerged as one of the most promising photovoltaic technologies owing to their outstanding optoelectronic properties, including high absorption coefficients, tunable bandgaps, long carrier diffusion lengths, and low fabrication costs. These hybrid organic-inorganic compounds offer high power conversion efficiencies, making them promising alternatives to conventional silicon-based solar cells. Despite the remarkable progress achieved in PSCs, their performance remains limited by incomplete utilization of the solar spectrum and various carrier recombination losses. Furthermore, the presence of lead in many high-performance PSCs raises significant environmental and health concerns, making the transition toward lead-free perovskite materials an essential research direction. To overcome the limitations of single-junction solar cells, including the Shockley-Queisser limit, multilayer absorber structures have been proposed as an effective strategy for broadening spectral absorption and enhancing photovoltaic conversion efficiency by combining materials with complementary bandgaps. In this context, the present thesis focuses on the numerical modeling and optimization of lead-free perovskite solar cells using the SCAPS-1D simulation software. The study begins with the analysis of a reference single-layer device based on K_2LiAlI_6. To overcome the limited spectral absorption of this single-layer configuration, we propose a bilayer architecture by introducing $RbGeBr_3$ as a second absorber layer, aiming to enhance light absorption across a broader spectral range. Subsequently, a third absorber layer, $FA_4GeSbCl_{12}$, is incorporated to develop a novel trilayer graded-bandgap configuration

(K_2LiAlI_6/$RbGeBr_3$/$FA_4GeSbCl_{12}$). In addition, several hole transport layer (HTL) materials are investigated, and the thickness and doping concentration of each absorber layer are systematically optimized to achieve superior photovoltaic performance. The objective of this work is to improve the efficiency of environmentally friendly lead-free perovskite solar cells and to evaluate the effectiveness of graded-bandgap multilayer architectures for maximizing solar spectrum utilization and enhancing power conversion efficiency.

This thesis is organized into three chapters as follows:

Chapter 1: provides a comprehensive overview of the principles underlying solar energy conversion, covering topics such as solar irradiation characteristics, the photovoltaic effect, semiconductor physics, and the behavior of p-n junctions. It further delves into the core operating mechanisms of solar cells, examining their performance metrics (J_{sc}, V_{oc}, FF, PCE) and the various loss mechanisms that limit efficiency. The chapter concludes with a detailed survey of different solar cell technologies, with a particular focus on emerging perovskite solar cells.

Chapter 2: defines the key materials used in this work and their chemical compositions, including the lead-free perovskite absorber materials: K_2LiAlI_6 (potassium lithium aluminum iodide), $RbGeBr_3$ (Rubidium Germanium Bromide), and $FA_4GeSbCl_{12}$ (Formamidinium Germanium Antimony halide). In addition to the most famous and widely used metal, gold (Au), as well as Copper iodide (CuI), which has proven to be highly effective as a hole transport layer (HTL). The SCAPS-1D simulation tool is also explained in detail, highlighting the essential physical equations governing semiconductor device simulation.

Chapter 3: presents and discusses the numerical simulation results obtained in this study. It begins with the validation of the simulation model by comparing the reference single-layer K_2LiAlI_6 device with previously reported data. The chapter then presents a comparative performance analysis of single-layer, bilayer, and trilayer configurations. Subsequently, a systematic optimization is carried out, including the selection of the optimal HTL from ten different materials, followed by the optimization of acceptor density and thickness for each absorber layer (K_2LiAlI_6, $RbGeBr_3$, and $FA_4GeSbCl_{12}$). The final optimized device configuration is presented, and its performance is compared with previous configurations. The chapter concludes with a summary of the key findings.

Chapter 01: Fundamentals of Solar Cells

1.1. Introduction

A solar cell is a technology that converts sunlight directly into electrical energy and represents one of the most significant achievements in renewable energy. The origins of this technology date back to the 19th century, when French physicist Alexandre Edmond Becquerel observed that illuminating certain electrical cells with sunlight generates an electric current. Since this pioneering discovery, solar cell technology has undergone continuous development, leading to various types of cells including crystalline silicon, compound semiconductors, organic cells, and perovskite solar cells. The operating principle of a solar cell is based on the photovoltaic effect, where photon absorption generates electron-hole pairs, converting light energy into electricity. Key performance parameters include open-circuit voltage (V_{oc}), short-circuit current (I_sc), fill factor (FF), and power conversion efficiency (η). This chapter provides the theoretical foundation for the study of photovoltaic solar cells. It introduces the fundamentals of solar radiation, the operating principles of illuminated p-n junctions, equivalent circuit models, and the main loss mechanisms affecting device performance. The chapter also presents an overview of the different types of solar cells, including first-generation (silicon-based), second-generation (thin-film), and third-generation (emerging) technologies. Particular attention is given to perovskite solar cells (PSCs), which have attracted considerable scientific interest due to their remarkable optoelectronic properties and rapidly increasing efficiencies, making them strong candidates for next-generation photovoltaic applications.

1.2. Fundamentals of Solar Radiation

1.2.1. Solar Energy and the Sun as an Energy Source

Solar energy constitutes the primary source of energy available on Earth and represents the driving force behind numerous natural and environmental processes. The Sun continuously releases vast amounts of energy through thermonuclear fusion reactions occurring in its core, where hydrogen nuclei combine to form helium while liberating significant quantities of electromagnetic radiation. This radiation propagates through space and reaches the Earth in the form of solar irradiance, which can be harvested and converted into useful electrical energy by photovoltaic devices. The amount of solar power received per unit area on a surface perpendicular to the solar rays at the outer boundary of the Earth's atmosphere is referred to as the solar constant. This parameter serves as a fundamental reference in solar energy studies and photovoltaic system design, as it represents the maximum available solar energy before atmospheric attenuation effects occur [1,3] which is quantified as:

$$I_{sc} \approx 1361\, W/m^2$$

1.2.2. Solar Spectrum

The solar radiation emitted by the Sun can be approximated as a blackbody radiator operating at a temperature of about 5800 K. The solar spectrum reaching the Earth is broadly distributed into three main optical wavelengths:

Ultraviolet (UV) Radiation: Accounts for approximately 7% of the total spectrum (characterized by short wavelengths and high photon energy).

Visible Light: Comprises around 47% of the spectrum (spanning the wavelength range from 400 nm to 700 nm.

Infrared (IR) Radiation: Constitutes about 46% of the spectrum (characterized by lower photon energies and longer wavelengths).[3]

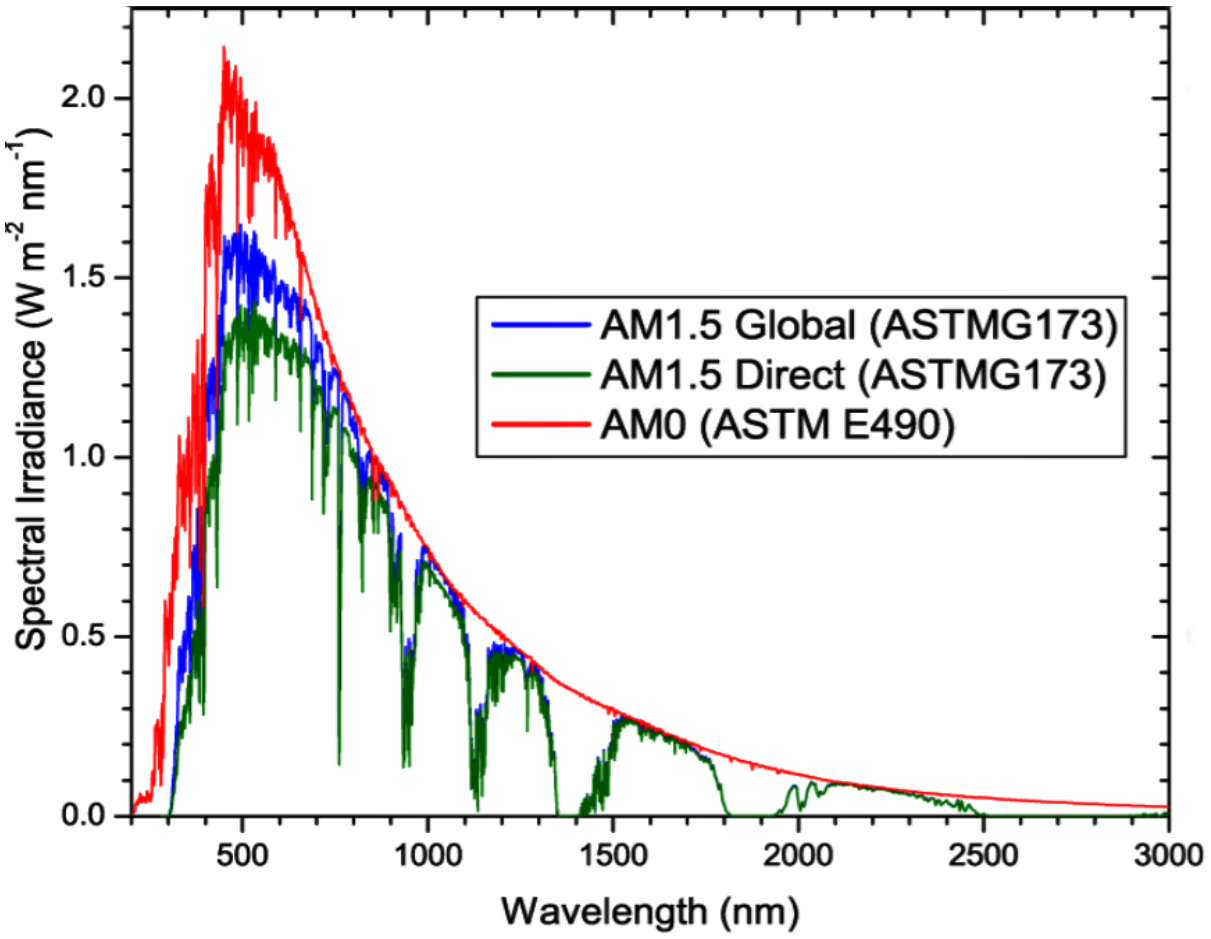

Figure 1.1: Spectral radiation curve illustrating the characteristics of the solar spectrum.

1.2.3. Air Mass (AM) Concept and Standard Test Conditions

As solar radiation travels through the Earth's atmosphere, it undergoes absorption and scattering processes caused by atmospheric gases, aerosols, and suspended particles. The extent of these interactions depends on the optical path length traversed by sunlight before reaching

the Earth's surface. To quantify this effect, the Air Mass (AM) parameter is introduced as a measure of the relative atmospheric path length compared to the shortest possible path when the Sun is positioned directly overhead. It is mathematically expressed as:

$$AM = \frac{1}{\cos(\theta_z)} \tag{1.1}$$

Where (θ_z) represents the solar zenith angle.

AM0: The solar spectrum outside the atmosphere, utilized primarily for satellite and space applications.

AM1: Represents the condition of sunlight falling perpendicularly on the Earth's surface

AM1.5: The standard spectrum designated for terrestrial applications, representing a solar path where the zenith angle is $(\theta_z) = 48.2^{\circ}$

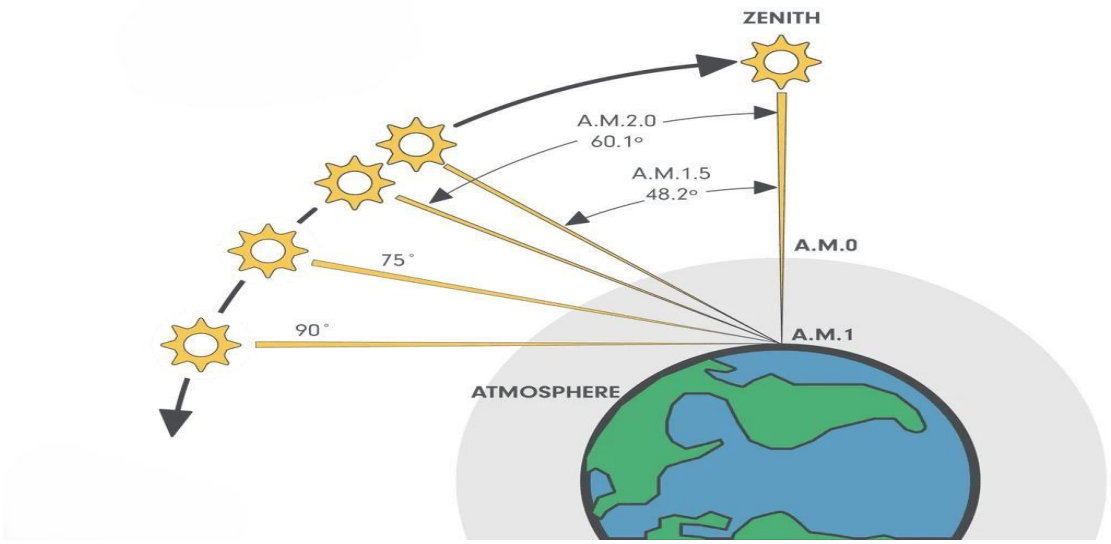

Figure 1.2: Atmospheric path geometry illustrating the Air Mass (AM) concept and the increase in solar radiation path length with increasing solar zenith angle

Standard Test Conditions (STC):

To evaluate and compare the performances of different solar cells uniformly across global research and manufacturing facilities, devices are tested under strict Standard Test Conditions (STC):

Irradiance: 1000 W/m^2

Spectral Distribution: AM1.5G (where 'G' denotes Global irradiance).

Cell Temperature: 25ºC.

The adoption of these standardized conditions enables meaningful comparisons between different photovoltaic technologies and ensures the reproducibility of experimental results obtained in research laboratories and industrial testing facilities worldwide [3].

1.3.Fundamentals of Photovoltaic Solar Cells

1.3.1. Definition and Concept of Solar Cells

A photovoltaic (PV) solar cell is a semiconductor device capable of directly converting sunlight into electrical energy through the photovoltaic effect. Unlike conventional power generation technologies that rely on mechanical motion or thermal cycles, photovoltaic conversion occurs entirely within a solid-state structure. When exposed to solar radiation, the device absorbs photons and generates electrical charge carriers that can be collected as useful electric current. Owing to their reliability, silent operation, low maintenance requirements, and environmental sustainability, photovoltaic cells have become one of the most important technologies for renewable electricity generation [2,6].

1.3.2. Historical Development of Photovoltaic Technology

The evolution of photovoltaic technology has been shaped by a succession of scientific discoveries and technological innovations that have significantly improved the efficiency and practicality of solar energy conversion. From the first observation of the photovoltaic effect to the emergence of advanced photovoltaic materials, each milestone has contributed to the development of modern solar cell technologies. The most important stages in the historical development of photovoltaics are summarized as follows:

1839: Alexandre Edmond Becquerel discovered the photovoltaic effect during experiments with illuminated electrolytic cells.

1873: Willoughby Smith discovered the photoconductive properties of selenium.

1883: Charles Fritts fabricated the first solid-state solar cell using selenium and a thin gold layer.

1905: Albert Einstein explained the photoelectric effect, establishing the theoretical basis of photovoltaic conversion.[6]

1954: Daryl Chapin, Calvin Fuller, and Gerald Pearson developed the first practical crystalline silicon solar cell at Bell Laboratories.

1958: Solar cells were successfully used aboard the Vanguard 1 satellite, marking the beginning of space photovoltaic applications.

1970s: The global energy crisis accelerated research and investment in photovoltaic technologies.

2009: Kojima et al. introduced the first perovskite solar cell with a power conversion efficiency of 3.8%.[11]

Present Day: Perovskite solar cells have achieved certified efficiencies exceeding 27%, making them among the most promising next-generation photovoltaic technologies [5,16].

These remarkable achievements reflect the continuous evolution of solar cell technology, from initial ideas and concepts to advanced applications in the field of solar energy.

1.3.3. Photovoltaic Energy Conversion Mechanism

The photovoltaic conversion process is based on the interaction between incident solar radiation and the semiconductor material of the solar cell. The transformation of light energy into electrical energy occurs through three fundamental steps:

Photon Absorption: When photons with energies equal to or greater than the semiconductor bandgap ($h\nu \geq E_g$) strike the absorber layer, they transfer their energy to electrons in the valence band, promoting them to the conduction band and generating electron–hole pairs.

Charge Carrier Separation: The photogenerated electrons and holes are separated by the built-in electric field established within the p–n junction. This separation prevents immediate recombination and directs the charge carriers toward opposite sides of the device.

Charge Carrier Collection: The separated charge carriers are transported to the corresponding electrical contacts, where they are collected and extracted through an external circuit, producing a direct electric current that can be delivered to a load.

The efficiency of a photovoltaic device depends strongly on the effectiveness of these three processes. Any losses associated with incomplete photon absorption, carrier recombination, or inefficient charge collection lead to a reduction in the overall power conversion efficiency of the solar cell [2,7].

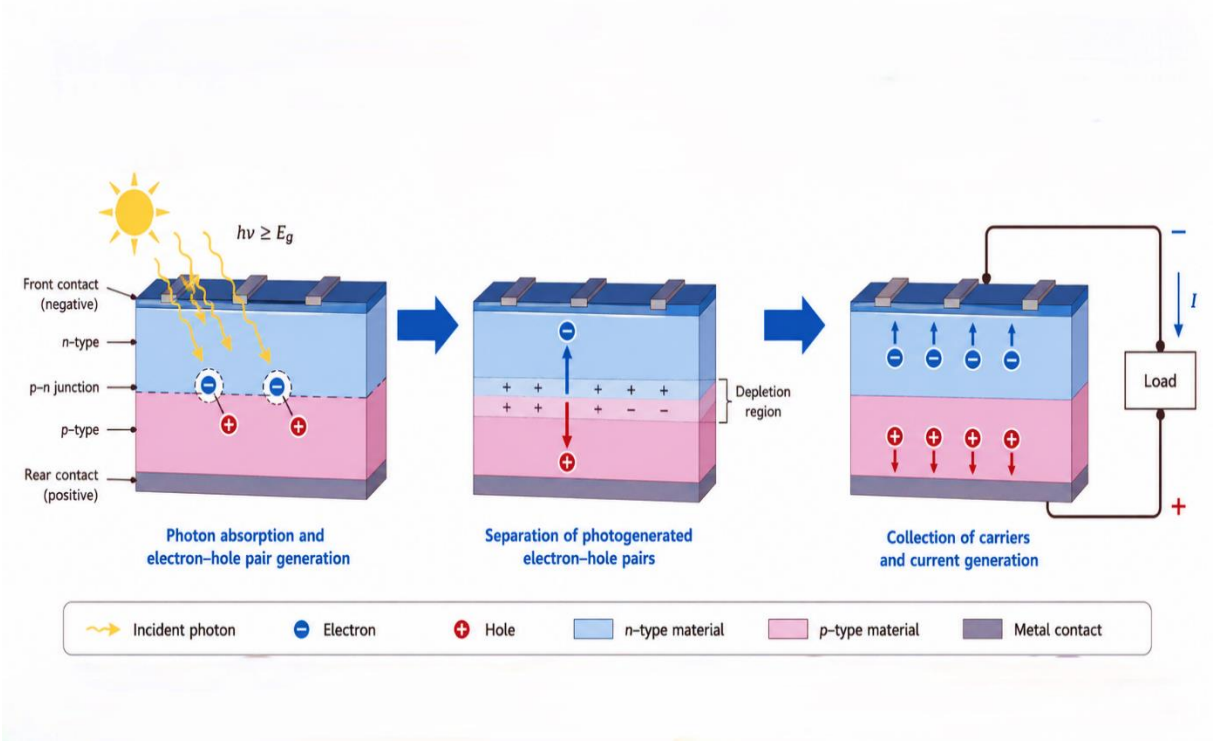

Figure 1.3: Three-step photovoltaic energy conversion mechanism in a solar cell.

1.3.4. Operating Principle of Solar Cells

The operating principle of a photovoltaic solar cell is based on the behavior of an illuminated p–n junction. When p-type and n-type semiconductor materials are brought into contact, charge carriers diffuse across the junction due to concentration gradients, resulting in the formation of a depletion region and an associated built-in electric field. Under solar illumination, photons absorbed within the semiconductor generate electron–hole pairs. The built-in electric field then separates these photogenerated carriers by driving electrons toward the n-type region and holes toward the p-type region, thereby reducing the probability of recombination. As charge carriers accumulate at the respective contacts, a potential difference is established across the device terminals. When an external circuit is connected, electrons flow through the load from the n-side to the p-side, generating an electric current and delivering electrical power. This direct conversion of solar energy into electrical energy through the combined processes of carrier generation, separation, and collection constitutes the fundamental operating mechanism of photovoltaic solar cells [2,7]. Figure 1. 4 illustrates the fundamental operating principle of a p–n junction solar cell under illumination.

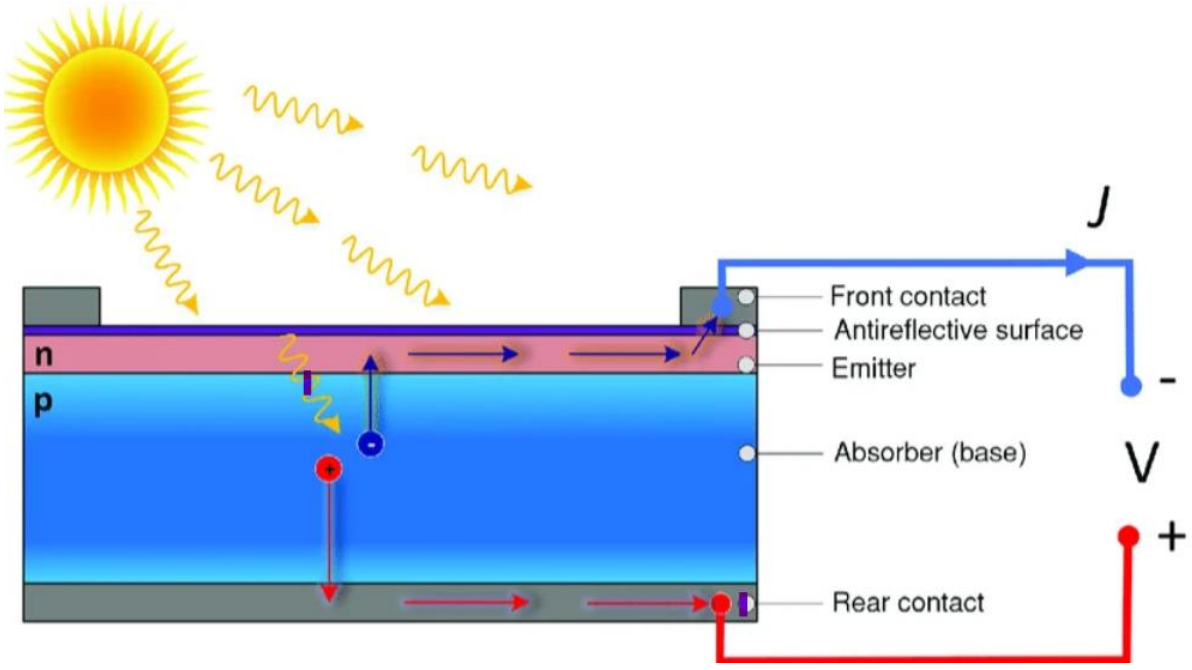

Figure 1.4: A cross-sectional diagram of a p-n junction solar cell illustrating the photovoltaic process

1.3.5. Semiconductor Materials and Energy Band Structure

Semiconductors are defined by an energy bandgap (E_g) that isolates the filled valence band from the empty conduction band at absolute zero. Semiconductors are classified according to the alignment of their band edges in momentum (k) space: [6,7]

Table 1.1. Comparison of Direct and Indirect Bandgap Semiconductors.

Semiconductor Type	**Electronic Transition Mechanism**	**Optical Properties**	**Examples**
Direct Bandgap	The valence band maximum and conduction band minimum align at the same crystal momentum vector (k).	Strong and rapid optical absorption; requires thin layers (few microns) to absorb sunlight.	Gallium Arsenide (GaAs), Perovskites ($MAPbI_3$).
Indirect Bandgap	The band extrema do not align at the same momentum; transition requires assistance from a phonon (lattice vibration).	Weak optical absorption edge; requires thicker absorber layers to ensure sufficient light capture.	Crystalline Silicon (c-Si), Germanium (Ge).

1.3.6. Illuminated P-N Junction Behavior

In the dark, the p-n junction exhibits standard rectifying diode behavior. Under illumination, the light-induced photogenerated current (I_{ph}) flows in the direction opposite to the forward-biased diode current. The total ideal current I passing through the cell is described by the ideal diode equation:

$$I = I_0 \left[exp\left(\frac{qV}{nk_BT}\right) - 1 \right] - I_{ph} \quad (1.2)$$

The illuminated current–voltage characteristics of a solar cell form the foundation for defining the principal performance parameters used to evaluate photovoltaic devices. These parameters provide quantitative measures of the cell's electrical behavior and energy conversion capability under specified operating conditions. The most important of these performance indicators are presented and discussed in the following section [7].

1.4. Performance Parameters of Solar Cells

The performance of a photovoltaic solar cell is evaluated through a set of electrical parameters derived from its current–voltage (I–V) characteristics under illumination. These parameters provide quantitative information about the cell's ability to generate electrical power and convert

incident solar energy into useful electricity. The most important performance indicators include the current–voltage and power–voltage characteristics, short-circuit current density, open-circuit voltage, maximum power point, fill factor, and power conversion efficiency [4,9].

1.4.1. Current–Voltage (I-V) Characteristics

The current–voltage (I–V) characteristic curve represents the fundamental electrical behavior of a solar cell under specified illumination conditions. It describes the relationship between the output current and terminal voltage and serves as the primary tool for evaluating photovoltaic performance. The curve extends from the short-circuit condition, where the current reaches its maximum value at zero voltage, to the open-circuit condition, where the voltage reaches its maximum value at zero current. Several important performance parameters, including the short-circuit current density, open-circuit voltage, maximum power point, fill factor, and conversion efficiency, can be extracted directly from the I–V characteristic [4,9].

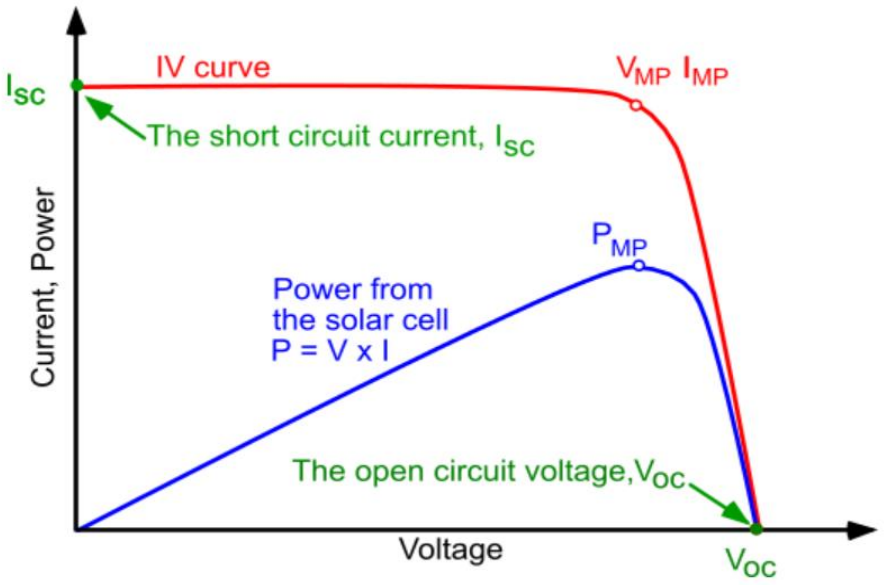

Figure 1.5: Typical current-voltage (I-V) characteristic curve of an illuminated solar cell

1.4.2. Power–Voltage (P-V) Characteristics

The power–voltage (P–V) characteristic curve illustrates the variation of the electrical power generated by a solar cell (P = I ×V) as a function of voltage. The power increases from zero at short-circuit conditions, reaches a maximum value at the Maximum Power Point (MPP), and then decreases to zero at the open-circuit voltag [4]. Jsc = Isc / A

1.4.3. Short-Circuit Current Density (Jsc)

The short-circuit current density (Jsc) is the current density generated by a solar cell when the terminal voltage is zero. It represents the maximum photocurrent produced under

illumination and depends on the incident photon flux, light absorption, and charge carrier collection efficiency [4,9].

$$J_{SC} = qG(L_n + L_p) \quad (1.3)$$

Where:

• G is the generation rate.

• L_n is the electron diffusion length.

• L_p is the hole diffusion length.

The short-circuit current density (Jsc) is related to the short-circuit current (Isc) through the active area of the solar cell. The relationship is expressed as:

$$I_{SC} = J_{SC} \times A \quad (1.4)$$

1.4.4. Open-Circuit Voltage (Voc)

The open-circuit voltage (V_{oc}) is the maximum voltage generated by a solar cell when no external current flows through the circuit (I = 0). It reflects the ability of the device to establish an electrical potential under illumination and is influenced by the semiconductor bandgap and carrier recombination mechanisms [4,7].

$$V_{OC} = \frac{nKT}{q}\, l_n \left(\frac{I_{ph}}{I_0} + 1\right) \quad (1.5)$$

where:

Voc : Open-circuit voltage (V).

n : Diode ideality factor.

k : Boltzmann constant (1.38×10^{-23} J·K^{-1}).

T : Absolute temperature (K).

q : Elementary charge (1.602×10^{-19} C).

Iph : Photogenerated current (A).

I0 : Reverse saturation current (A)

1.4.5. Maximum Power Point (MPP)

The Maximum Power Point (MPP) is the operating point at which a solar cell delivers its maximum electrical power output. It is defined by the voltage (V_{mp}) and current (I_{mp}) corresponding to the highest point on the P–V curve [4].

$$P_{max} = V_{mp} + I_{mp} \quad (1.6)$$

where:

P_{max} : Maximum output power (W).

V_{mp} : Voltage at the maximum power point (V).

I_{mp} : Current at the maximum power point (A).

1.4.6. Fill Factor (FF)

The Fill Factor (FF) is a measure of the quality of a solar cell and the squareness of its current–voltage characteristic. It is defined as the ratio between the maximum obtainable power and the theoretical power determined from the open-circuit voltage and short-circuit current [4,9].

$$FF = \frac{V_{mp} \cdot I_{mp}}{V_{oc} \cdot I_{sc}} \tag{1.7}$$

where:

FF : Fill factor.

V_{mp} : Voltage at the maximum power point (V).

I_{mp} : Current at the maximum power point (A).

V_{oc} : Open-circuit voltage (V).

I_{sc} : Short-circuit current (A).

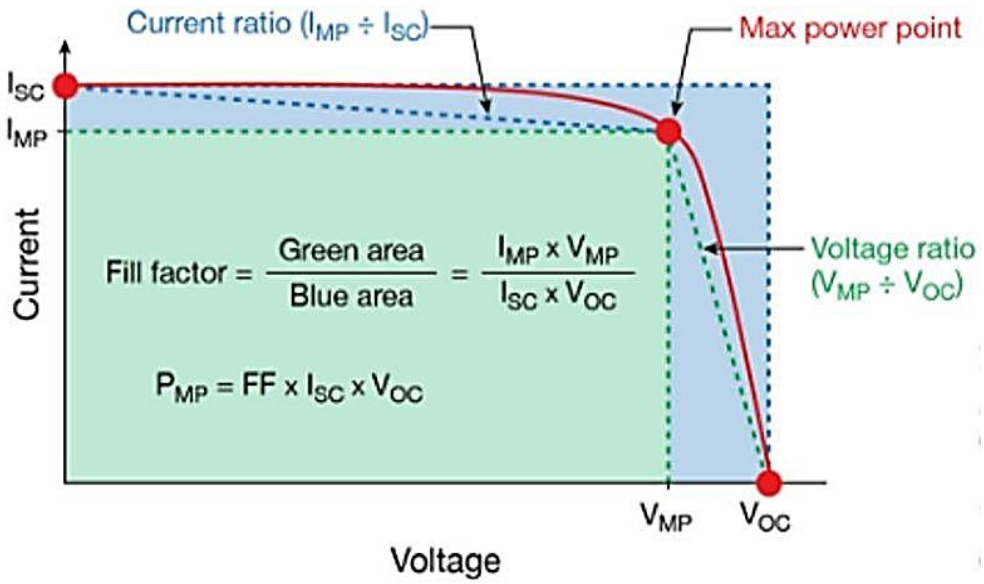

Figure 1.6: Fill Factor (FF) of a Solar Cell.

1.4.7. Power Conversion Efficiency (PCE)

The Power Conversion Efficiency (PCE), denoted by η, represents the percentage of incident solar energy converted into useful electrical energy. It is the most widely used parameter for evaluating the performance of photovoltaic devices:

$$\eta = \frac{P_{max}}{P_{in}} \times 100 = \frac{V_{oc} \cdot I_{sc} \cdot FF}{P_{in}} \times 100 \tag{1.8}$$

The performance parameters discussed above provide a quantitative evaluation of photovoltaic devices under illumination. However, a deeper understanding of solar cell operation and loss mechanisms requires the use of equivalent electrical circuit models. These models facilitate the analysis of current transport and device behavior and are presented in the following section [4,9].

1.5. Electrical Modeling of Solar Cells

To analyze and predict the electrical behavior of photovoltaic devices under various operating conditions, solar cells are commonly represented using equivalent electrical circuit models. These models provide a simplified description of the physical processes occurring within the device and enable the evaluation of important performance parameters. Among the different approaches available in the literature, the ideal solar cell model and the single-diode equivalent circuit are the most widely used for photovoltaic analysis [7,8].

1.5.1. Ideal Solar Cell Model

The ideal solar cell model represents the simplest electrical description of a photovoltaic device. It consists of a constant photocurrent source connected in parallel with an ideal p–n junction diode. In this model, all resistive losses and recombination effects are neglected, allowing the fundamental photovoltaic behavior to be analyzed under ideal operating conditions [7].

1.5.2. Single-Diode Equivalent Circuit

Since practical solar cells exhibit non-ideal behavior, a more realistic representation is provided by the single-diode model. This model extends the ideal circuit by including a series resistance (Rs) and a shunt resistance (Rsh), which account for internal resistive losses and leakage currents, respectively. Owing to its good balance between simplicity and accuracy, the single-diode model is widely used for the analysis and simulation of photovoltaic devices [7, 8].

The output current of the solar cell is expressed as:

$$I = I_{ph} - I_0 \left[exp\left(\frac{q(V + IR_s)}{nkT} \right) - 1 \right] - \frac{V + IR_s}{R_{sh}} \quad (1.9)$$

where:

I : Output current (A).

I_{ph} : Photogenerated current (A).

I_0 : Reverse saturation current (A).

V : Output voltage (V).

R_s : Series resistance (Ω).

R_{sh} : Shunt resistance (Ω).

q : Elementary charge (C).

n : Diode ideality factor.

k : Boltzmann constant ($J \cdot K^{-1}$).

T : Absolute temperature (K).

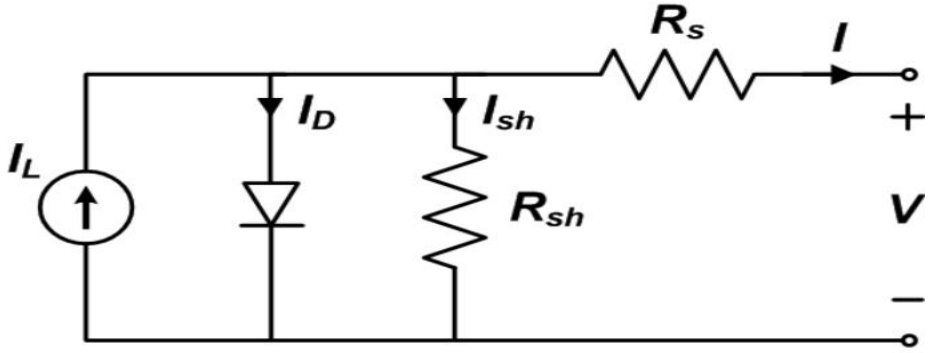

Figure 1.7: Single-diode equivalent circuit model of a solar cell.

1.5.3. Influence of Series (Rs) and Shunt (Rsh) Resistances

Series Resistance (R_s): Originates from bulk material resistance and contact resistance. Ideally, it should approach zero ($R_s \rightarrow 0$). Increasing R_s heavily degrades the FF.

Shunt Resistance (R_{sh}): Caused by structural crystal defects and impurities. Ideally, it should approach infinity($R_s \rightarrow \infty$). Low values of R_{sh} cause severe current leakage, causing a sharp drop in both V_{oc} and FF [7].

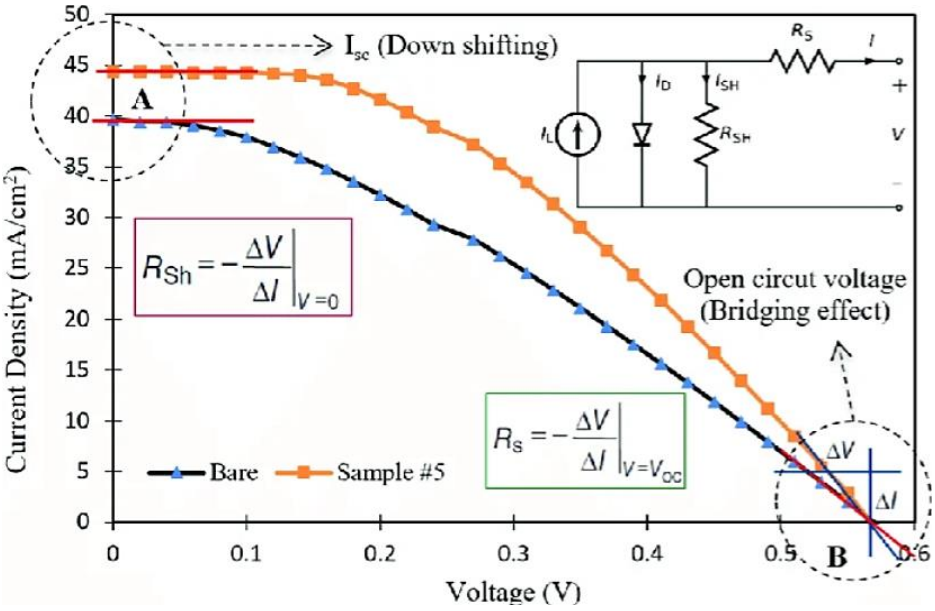

Figure 1.8: Effect of series resistance (Rs) and shunt resistance (Rsh) on the I–V characteristics of a solar cell.

1.6. Quantum Efficiency and Spectral Response

Quantum efficiency and spectral response are important parameters used to evaluate the ability of a solar cell to convert incident photons into electrical charge carriers. These quantities provide valuable information about the optical and electrical performance of photovoltaic devices over different wavelength ranges [9].

1.6.1. Quantum Efficiency Concept

Quantum Efficiency (QE) is a measure of the ability of a solar cell to convert incident photons into collected charge carriers. It is defined as the ratio of the number of charge carriers collected by the device to the number of photons incident on its surface at a given wavelength(λ). Quantum efficiency provides valuable information about the effectiveness of photon absorption, charge generation, and carrier collection processes within the solar cell [9].

1.6.2. External Quantum Efficiency (EQE)

External Quantum Efficiency (EQE) represents the ratio of collected charge carriers to the total number of photons incident on the solar cell surface. It includes the effects of optical losses such as reflection and transmission and is commonly used to evaluate the wavelength-dependent performance of photovoltaic devices [9].

$$\mathrm{EQE}(\lambda) = \frac{\text{Number of collected electron} - \text{hole pairs}}{\text{Number of incident photons}} = \frac{I_{SC}}{P_{in}} \cdot \frac{hc}{q\lambda} \qquad (1.10)$$

Where P_{in} is incident power, I_{sc} is Short circuit current, h is Planck constant (6.626× 10-34 J.s), λ is wavelength of the incident photons, and c is speed of light (2.998×108 m/s).

1.6.3. Internal Quantum Efficiency (IQE)

Internal Quantum Efficiency (IQE) represents the ratio of collected charge carriers to the number of photons that are actually absorbed within the active layer of the solar cell. Unlike EQE, it excludes optical losses due to reflection and transmission, providing a more accurate assessment of the electrical performance of the device [9].

$$IQE(\lambda) = \frac{Number\ of\ collected\ electron - hole\ pairs}{Number\ of\ absorber\ photons} = \frac{EQE(\lambda)}{1 - R(\lambda)} \qquad (1.11)$$

where R is the reflection coefficient from the top surface of solar cell.

1.6.4. Spectral Response Analysis

Spectral Response (SR) describes the sensitivity of a solar cell to light of different wavelengths and is defined as the ratio of the generated photocurrent to the incident optical power at a specific wavelength. It is commonly expressed in amperes per watt (A/W) and provides valuable information about the wavelength range over which the solar cell effectively converts light into electricity.

$$SR(\lambda) = \frac{q \,.\, \lambda}{h \,.\, c} EQE(\lambda) \tag{1.12}$$

The quantum efficiency and spectral response characteristics provide valuable insights into the optical absorption and charge collection processes within photovoltaic devices. However, several loss mechanisms limit the conversion of absorbed solar energy into useful electrical power. These mechanisms are discussed in the following section.

1.7. Loss Mechanisms in Photovoltaic Devices

Single-junction solar cells are bound by the fundamental thermodynamic balance known as the Shockley-Queisser limit, which caps the maximum theoretical efficiency at roughly ≈33%due to several losses [10].

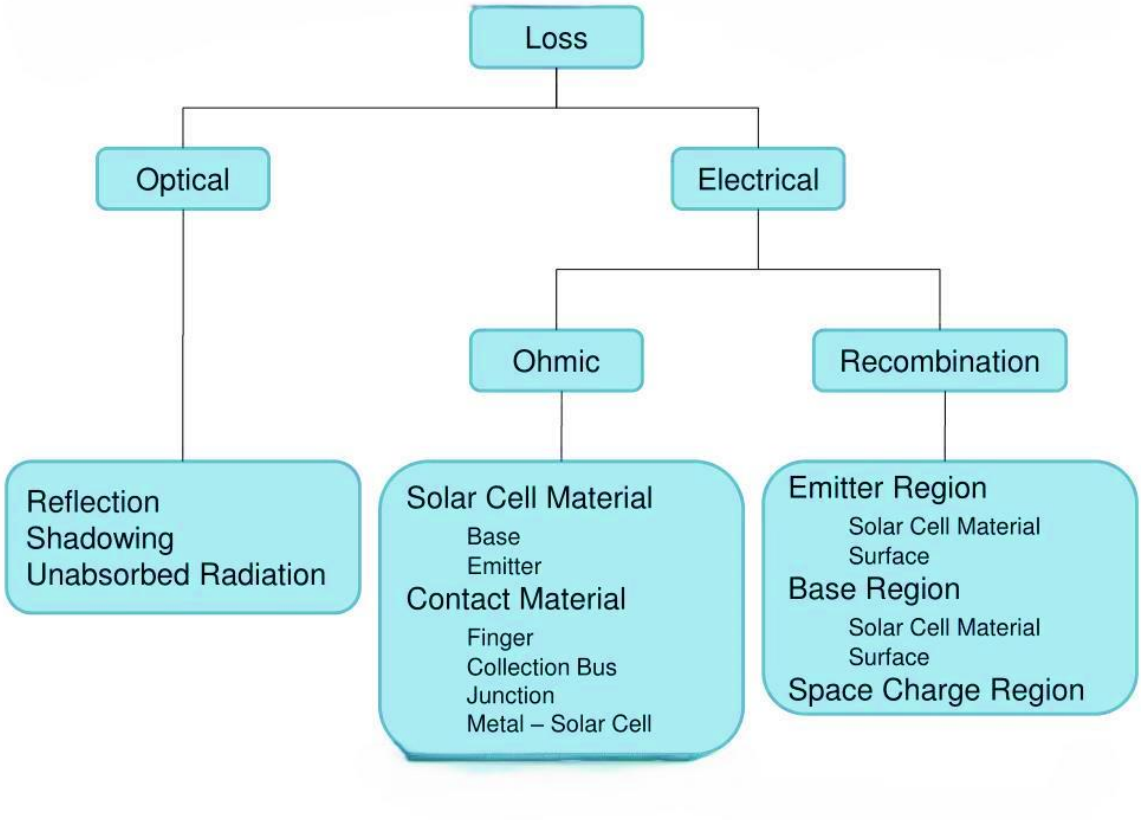

Figure 1.9: Major loss mechanisms in photovoltaic solar cells.

1.7.1. Optical Losses

Optical losses occur when incident solar radiation is not fully utilized by the solar cell. These losses result from light reflection at the cell surface, transmission through the absorber layer without absorption, and the inability of sub-bandgap photons to generate charge carriers. Furthermore, photons with energies exceeding the bandgap lose part of their energy as heat, reducing the overall photovoltaic conversion efficiency [9,10].

1.7.2. Recombination Losses

Recombination occurs when a light-generated carrier disappears before collection. It operates through three pathways:

Radiative Recombination: The direct band-to-band inversion of photon absorption.

Auger Recombination: A three-particle interaction where energy is given to another free carrier.

Shockley-Read-Hall (SRH) Recombination: A defect-mediated process where chemical impurities trap charge carriers [9,7].

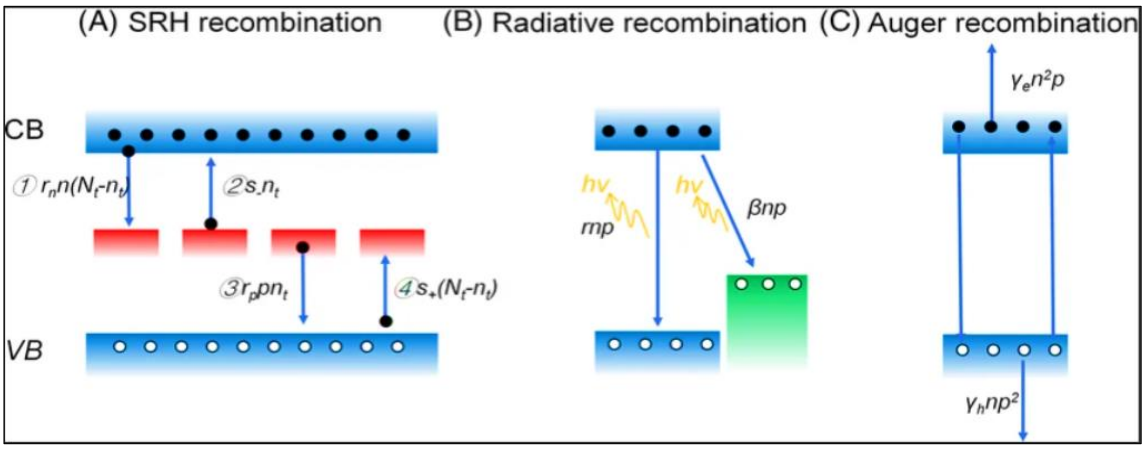

Figure 1.10: Mechanisms of primary charge carrier recombination in semiconductors

1.7.3. Resistive Losses

Resistive losses arise from the internal electrical resistances of the solar cell and lead to power dissipation in the form of heat. These losses are mainly associated with the series resistance (Rs) and shunt resistance (Rsh), which negatively affect the fill factor and overall device performance [7].

1.7.4. Thermalization Losses

When a semiconductor absorbs a high-energy photon (hv >> Eg), the electron is excited high into the conduction band and quickly loses this excess kinetic energy as heat through lattice vibrations until it reaches the conduction band edge [10].

1.8. Classification of Photovoltaic Technologies

Photovoltaic technologies have undergone significant development since the invention of the first solar cell and are commonly classified into three generations according to their materials, fabrication technologies, and performance characteristics. The first generation is based primarily on crystalline silicon wafers, the second generation includes thin-film technologies, while the third generation encompasses emerging photovoltaic concepts designed to achieve higher efficiencies and lower production costs. A comparison of the main characteristics of these photovoltaic generations is presented in Table 1.2 [1,5].

Table 1.2: Comprehensive Comparison of Photovoltaic Generations

Feature	**First-Generation**	**Second-Generation**	**Third-Generation**
Primary Base Material	High-purity wafer-based Crystalline Silicon (c-Si).	Thin-Film non-silicon or amorphous layers deposited on substrates.	Emerging advanced configurations, organics, and hybrid frameworks.
Dominant Sub-types	Monocrystalline (Mono-Si), Polycrystalline (Poly-Si).	Amorphous Silicon (a-Si), Cadmium Telluride (CdTe), CIGS.	Dye-Sensitized (DSSC), Organic (OPV), **Perovskite (PSC)**.
Max Certified Lab Efficiency	~ 26.1%.	~ 23.4%.	~ 26.1% (Single-junction Perovskite).
Key Advantages	Outstanding long-term stability and field maturity (>25 years).	Drastic material volume reductions, flexible, lightweight integrations.	Low temperature liquid processing, extremely low cost, tunable properties.
Primary Drawbacks	High manufacturing energy demands and thick material processing.	Concerns over elemental scarcity and toxic components (Cd).	Ongoing challenges with long-term atmospheric and thermal stability.

Among the third-generation photovoltaic technologies, perovskite solar cells have attracted considerable attention due to their remarkable optoelectronic properties, low-temperature fabrication processes, and rapidly increasing power conversion efficiencies. Consequently, they

are considered one of the most promising candidates for next-generation photovoltaic applications.

1.9. Emerging Perovskite Solar Cells (PSCs)

Perovskite solar cells (PSCs) have emerged as one of the most promising photovoltaic technologies owing to their exceptional optoelectronic properties and rapid progress in power conversion efficiency. Since their introduction in photovoltaic applications, PSCs have attracted significant research interest due to their low-cost fabrication, tunable material properties, and compatibility with various device architectures. As a result, they are considered strong candidates for next-generation solar energy conversion systems [12,13].

1.9.1. Introduction to Perovskite Materials

The term "perovskite" refers to a class of materials that share the same crystal structure as calcium titanate ($CaTiO_3$). In photovoltaic applications, perovskite materials typically consist of hybrid organic–inorganic metal halides that exhibit excellent optical absorption and charge transport properties. These characteristics make them highly suitable as absorber layers in high-performance solar cells [11,12].

1.9.2. Structural and Optoelectronic Properties

Perovskite compounds follow the general stoichiometry **ABX_3**:

A: A large organic or inorganic monovalent cation located at the unit cell corners (e.g., Methylammonium ($CH_3NH_3^+$ *or* MA).

B: A divalent metal cation occupying the body center, typically Lead (Pb^{2+}).

X: A monovalent halogen anion coordinating the metal in an octahedron (e.g., Iodine (I^-)).

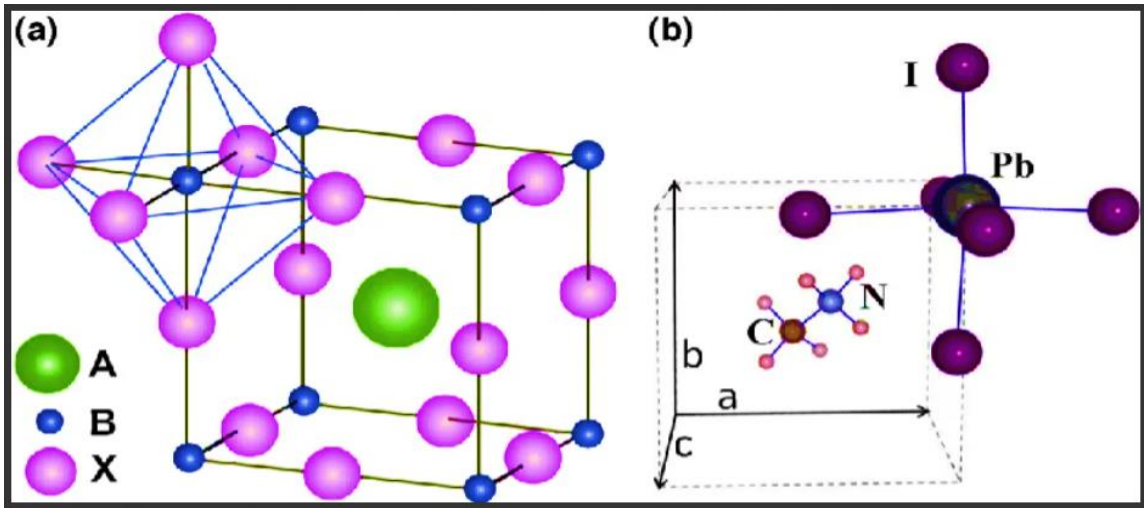

Figure 1.11: Three-dimensional model of the crystal lattice of the ABX3 perovskite unit cell

Unique Optoelectronic Advantages:

Exceptionally high optical absorption coefficients across visible spectrum boundaries.

Long carrier diffusion lengths enabling efficient collection of charges.

Tunable bandgaps (E_g) controllable via halide mixing [12,13].

1.9.3. Advantages of Perovskite Solar Cells

Perovskite solar cells offer several advantages that have contributed to their rapid development in recent years. These devices exhibit high optical absorption coefficients, long charge-carrier diffusion lengths, high carrier mobility, and tunable bandgaps, enabling efficient light harvesting and charge collection. In addition, their low-temperature and solution-based fabrication processes provide a cost-effective alternative to conventional silicon-based photovoltaic technologies. One of the most remarkable features of perovskite solar cells is the unprecedented improvement in their power conversion efficiency (PCE). Since their first application in photovoltaics in 2009, when an efficiency of approximately 3.8% [11] was reported, continuous advances in material engineering, interface optimization, and device architecture have resulted in a rapid increase in efficiency, exceeding 26% [5][16] in recent years. This exceptional progress highlights the strong potential of perovskite solar cells as one of the most promising candidates for next-generation photovoltaic technologies. Figure 1.12 illustrates the remarkable progress in the energy conversion efficiency of perovskite solar cells over the past decade.

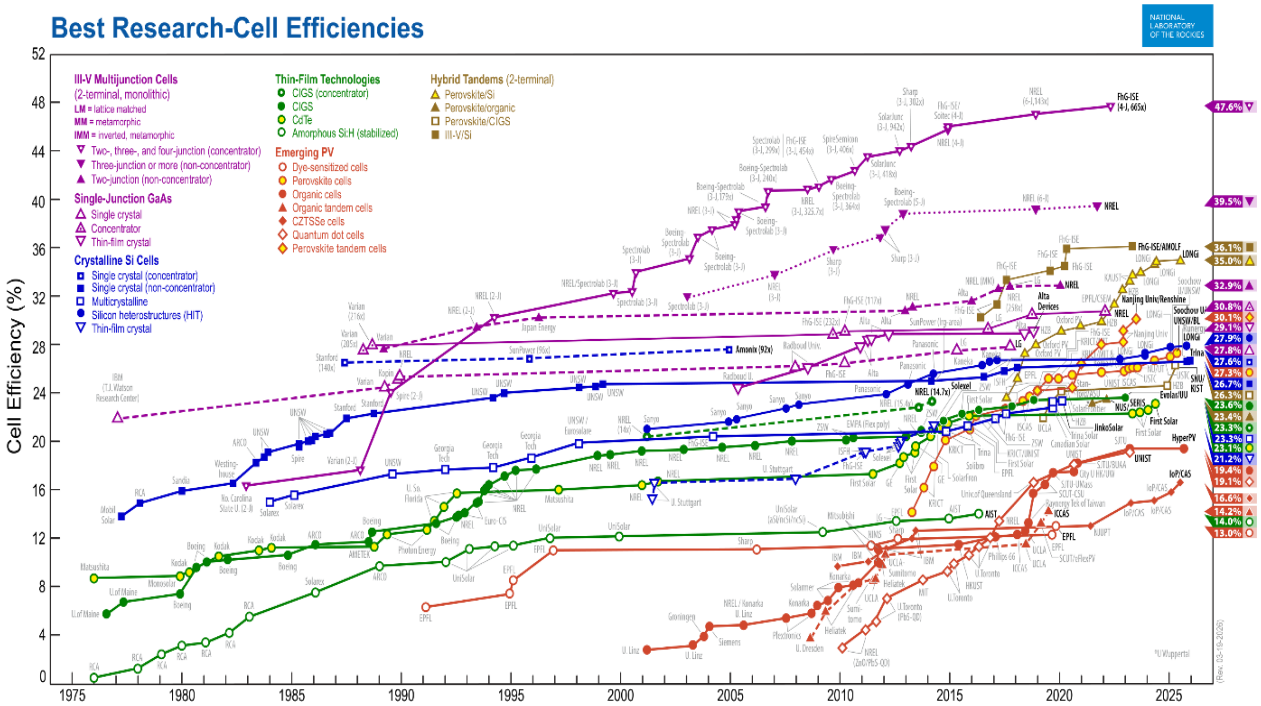

Figure 1.12: Evolution of the power conversion efficiency of perovskite solar cells compared with other photovoltaic technologies.

1.9.4. Current Challenges and Stability Issues

Despite their remarkable performance, perovskite solar cells still face several challenges that hinder large-scale commercialization. One of the main limitations:

Moisture and Oxygen Instability: The organic components are highly hygroscopic and readily degrade upon reacting with atmospheric water molecules.

Thermal and Photostability: Crystal phase transitions or ion migration can occur under prolonged exposure to solar heating.

Lead Toxicity: The presence of water-soluble lead (Pb) raises environmental and safety concerns, directing research toward lead-free alternatives like tin (Sn) [12,15].

1.10. Conclusion

This chapter presented the theoretical background of photovoltaic solar cells, including the fundamentals of solar radiation, semiconductor physics, photovoltaic energy conversion mechanisms, and the principal performance parameters used to evaluate solar cell operation. Electrical modeling approaches, quantum efficiency concepts, and the main loss mechanisms affecting photovoltaic performance were also discussed. Finally, an overview of photovoltaic technology generations was provided, with particular emphasis on perovskite solar cells and their unique properties, advantages, and current challenges. This theoretical foundation serves as the basis for the subsequent chapters of this work.

References Chapter 1

[1] Green, M. A. (2022). *Third generation photovoltaics: Advanced solar energy conversion* (2nd ed.). Springer.

[2] Nelson, J. (2020). *The physics of solar cells*. Imperial College Press.

[3] Kalogirou, S. A. (2024). *Solar energy engineering: Processes and systems* (4th ed.). Academic Press.

[4] Luque, A., & Hegedus, S. (2021). *Handbook of photovoltaic science and engineering* (3rd ed.). John Wiley & Sons.

[5] Green, M. A., Dunlop, E. D., Yoshita, M., Kopidakis, N., & Hao, X. (2025). Solar cell efficiency tables (Version 67). *Progress in Photovoltaics: Research and Applications, 33*(1), 3–12.

[6] Pierret, R. F. (2021). *Semiconductor device fundamentals*. Pearson.

[7] Sze, S. M., Ng, K. K., & Li, Y. (2021). *Physics of semiconductor devices* (4th ed.). John Wiley & Sons.

[8] Burgelman, M., Nollet, P., & Degrave, S. (2000). Modelling polycrystalline semiconductor solar cells. *Thin Solid Films, 361–362*, 527–532.

[9] Würfel, P., Würfel, U., & Brown, T. (2023). *Physics of solar cells: From basic principles to advanced concepts* (4th ed.). Wiley-VCH.

[10] Shockley, W., & Queisser, H. J. (1961). Detailed balance limit of efficiency of p–n junction solar cells. *Journal of Applied Physics, 32*(3), 510–519.

[11] Kojima, A., Teshima, K., Shirai, Y., & Miyasaka, T. (2009). Organometal halide perovskites as visible-light sensitizers for photovoltaic cells. *Journal of the American Chemical Society, 131*(17), 6050–6051.

[12] Correa-Baena, J.-P., Saliba, M., Buonassisi, T., Grätzel, M., Abate, A., Tress, W., & Hagfeldt, A. (2017). Promises and challenges of perovskite solar cells. *Science, 358*(6364), 739–744.

[13] Park, N.-G. (2024). Perovskite solar cells: Present status and future prospects. *Materials Today Energy*.

[14] Huang, J., et al. (2025). A review on perovskite/silicon tandem solar cells. *Energies, 18*(16), 4327.

[15] Shevaleevskiy, O. I. (2020). Perovskite solar cells: Recent progress and future prospects. *Nanosystems: Physics, Chemistry, Mathematics, 11*(6), 716–728.

[16] National Renewable Energy Laboratory (NREL). (2025). *Best research-cell efficiency chart*. National Renewable Energy Laboratory.

Chapter 02: Materials and SCAPS-1D Software

2.1. Introduction

Perovskite materials represent a key component in modern solar cells, playing an essential role in converting sunlight into electrical energy. These materials possess exceptional optoelectronic properties that make them highly efficient at light absorption and charge carrier transport. Typically, perovskite compounds exhibit a three-dimensional crystal structure and offer excellent light absorption across a broad portion of the solar spectrum, enabling them to achieve impressive power conversion efficiencies. Furthermore, the high carrier mobility of perovskite layers enhances the movement of both electrons and holes within the solar cell, contributing to improved device performance. The study and development of perovskite layers remain an active and promising field in renewable energy research, as their integration into solar cells marks a significant step toward improving the efficiency of photovoltaic energy conversion.

In this chapter, we define the perovskite materials used in this work, with particular emphasis on the lead-free absorber materials employed in our simulations: K_2LiAlI_6 (potassium lithium aluminum iodide), $RbGeBr_3$ (rubidium germanium bromide), and $FA_4GeSbCl_{12}$ (formamidinium germanium antimony). In addition, the other layer materials are described, including ITO as the front contact, TiO_2 as the electron transport layer (ETL), CuI as the hole transport layer (HTL), and Au as the back contact. Furthermore, we introduce the SCAPS-1D simulation software, discussing its main features, governing physical equations, and the methodology for conducting solar cell simulations. This will provide readers with a thorough understanding of the software and its application in this study.

2.2.Description Materials

2.2.1. Indium Tin Oxide (ITO)

Indium Tin Oxide (ITO) is employed as the transparent conductive front electrode in the proposed trilayer perovskite solar cell owing to its unique combination of high optical transparency and excellent electrical conductivity. The material is primarily composed of indium oxide (In_2O_3) doped with tin ions (Sn^{4+}), where the incorporation of tin significantly increases the free electron concentration and consequently enhances the electrical conductivity of the film. Due to its optical transparency exceeding 85% within the visible spectral region, ITO allows efficient transmission of incident solar radiation to the underlying active layers while simultaneously serving as an effective charge-collecting electrode. Furthermore, its low sheet resistance minimizes resistive losses during carrier transport, thereby improving the overall

electrical performance of the device. These characteristics make ITO one of the most widely used transparent conductive oxides in photovoltaic applications and an appropriate choice for the front contact layer in the proposed solar cell structure [3,4].

2.2.2. Titanium dioxide (TiO_2)

Titanium dioxide (TiO_2) is utilized as the electron transport layer (ETL) in the proposed device due to its favorable electronic properties, wide bandgap, and excellent chemical stability. With a bandgap of approximately 3.2 eV, TiO_2 exhibits high transparency to visible light, ensuring that most incident photons reach the absorber layers without significant optical losses. In addition, its conduction band position is well aligned with those of the perovskite absorber materials, facilitating efficient extraction and transport of photogenerated electrons toward the front electrode. At the same time, the large valence band offset acts as an effective barrier against hole transport, thereby suppressing charge recombination at the front interface. The electronic behavior of TiO_2 is primarily governed by titanium and oxygen ions within its crystal lattice, while intrinsic defects such as oxygen vacancies may contribute to n-type conductivity and enhance electron transport. Owing to these characteristics, TiO_2 plays a crucial role in improving charge separation efficiency, reducing interfacial recombination losses, and enhancing the overall photovoltaic performance of the proposed trilayer perovskite solar cell [5,6].

2.2.3. Potassium lithium aluminum iodide (K_2LiAlI_6)

K_2LiAlI_6 is employed as the wide-bandgap absorber layer in the proposed trilayer perovskite solar cell owing to its favorable optoelectronic properties, excellent structural stability, and environmentally friendly lead-free composition. As a halide double perovskite belonging to the $A_2BB'X_6$ family, the material exhibits a stable crystal structure composed of potassium (K), lithium (Li), aluminum (Al), and iodine (I), which contributes to its thermal and chemical robustness. K_2LiAlI_6 possesses a direct bandgap of approximately 1.73 eV, enabling efficient absorption of high-energy photons within the ultraviolet and short-wavelength visible regions of the solar spectrum. Furthermore, its strong optical absorption, low reflectivity, and favorable charge-transport characteristics promote efficient photocarrier generation and extraction. Within the proposed trilayer architecture, K_2LiAlI_6 serves as the upper absorber layer, where it selectively harvests high-energy photons while transmitting lower-energy photons toward the underlying absorbers. Recent SCAPS-1D simulations reported by Ayyaz et al. demonstrated that solar cells incorporating K_2LiAlI_6 as the absorber layer can achieve a power conversion efficiency (PCE) of approximately 22.05% under optimized operating conditions, highlighting its potential for advanced photovoltaic applications [7,8].

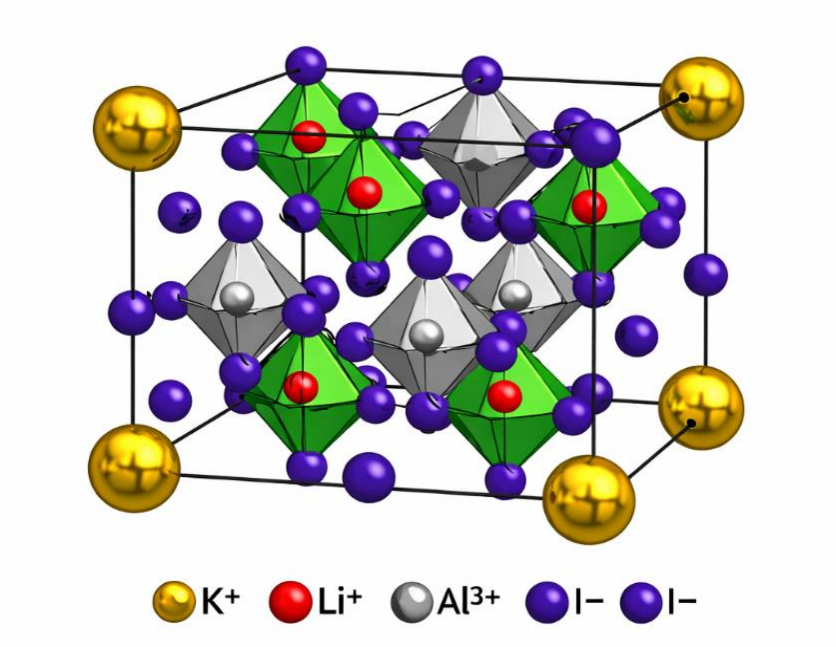

Figure 2.1: The crystal structure of unit cell of K_2LiAlI_6.

2.2.4. Rubidium Germanium Bromide ($RbGeBr_3$)

$RbGeBr_3$ is selected as the intermediate absorber layer due to its excellent optical and electrical properties as well as its lead-free composition. This inorganic perovskite material exhibits high structural stability and a suitable bandgap of approximately 1.49 eV, which allows efficient absorption of a large portion of the visible solar spectrum. In addition, the material possesses high carrier mobility and favorable energy-level alignment with adjacent transport and absorber layers, facilitating charge transfer and reducing interfacial energy losses. Within the proposed trilayer configuration, $RbGeBr_3$ functions as a bridge between the wide-bandgap K_2LiAlI_6 layer and the narrow-bandgap $FA_4GeSbCl_{12}$ layer, thereby enhancing spectral utilization and improving photocurrent generation. According to recent numerical investigations conducted using the SCAPS-1D simulator, optimized $RbGeBr_3$-based solar cells achieved a power conversion efficiency of up to 26.54%, demonstrating the material's strong potential for high-performance photovoltaic devices [9].

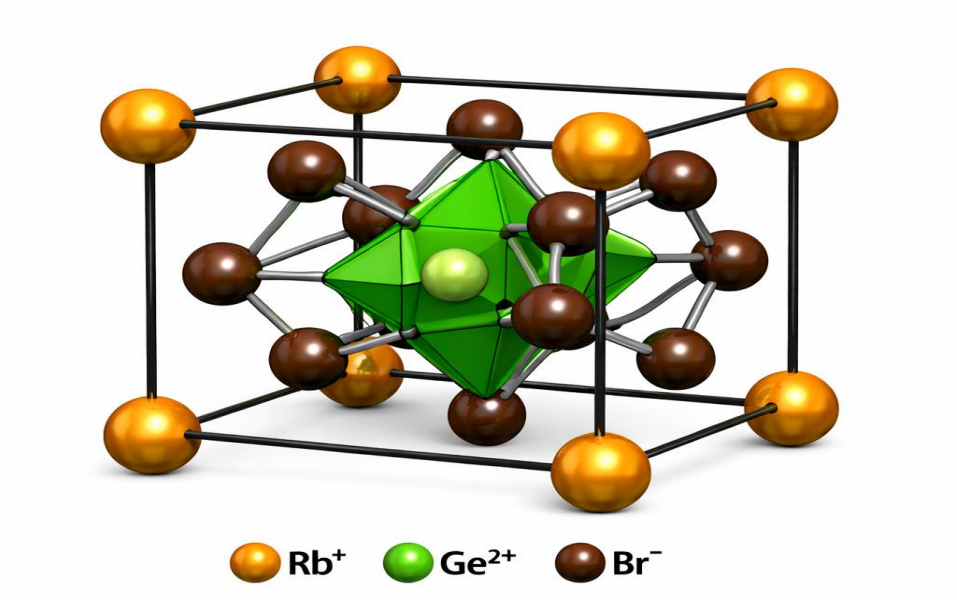

Figure 2.2: The crystal structure of unit cell of $RbGeBr_3$.

2.2.5. Formamidinium Germanium Antimony ($FA_4GeSbCl_{12}$)

$FA_4GeSbCl_{12}$ is a lead-free double perovskite material composed of formamidinium (FA), germanium (Ge), antimony (Sb), and chlorine (Cl), developed as an environmentally friendly alternative to conventional lead-based perovskites. It possesses a narrow bandgap of approximately 1.30 eV, enabling efficient absorption of visible sunlight and making it highly suitable for photovoltaic applications. The material exhibits excellent charge transport properties due to its high electron and hole nobilities, which facilitate efficient carrier collection. $FA_4GeSbCl_{12}$ also demonstrates favorable optoelectronic characteristics, including strong optical absorption and reduced recombination losses. Numerical simulations using SCAPS-1D have shown that solar cells based on this absorber can achieve remarkable power conversion efficiencies. An optimized Glass/FTO/ZnO/$FA_4GeSbCl_{12}$/Cu_2O/Au device structure achieved a power conversion efficiency (PCE) of 38.28%, with an open-circuit voltage (Voc) of 1.2153 V, a short-circuit current density (Jsc) of 35.03 mA/cm², and a fill factor (FF) of 89.91%. Furthermore, the material offers improved environmental compatibility by eliminating toxic lead components. These properties make $FA_4GeSbCl_{12}$ a promising candidate for next-generation high-efficiency and sustainable perovskite solar cells [10].

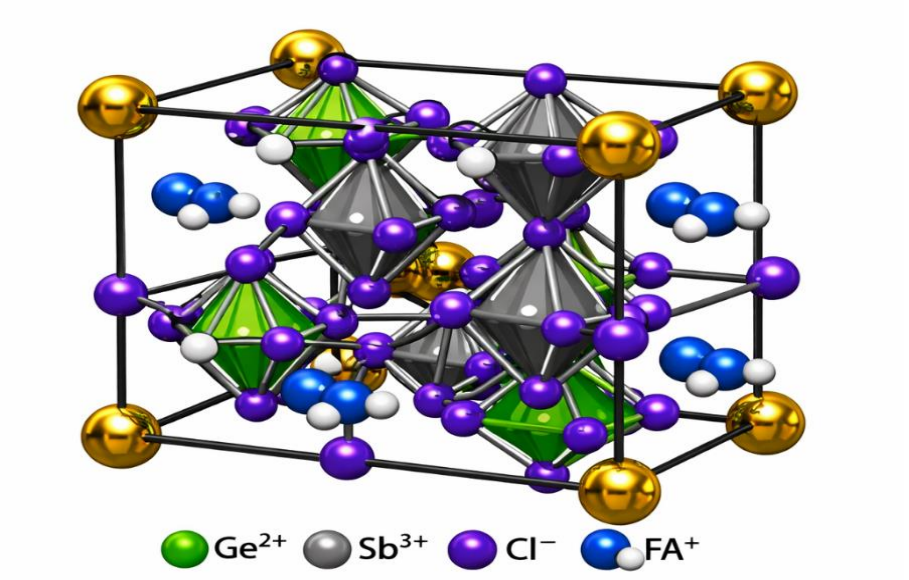

Figure 2.3: The crystal structure of unit cell of $FA_4GeSbCl_{12}$.

2.2.6. Copper iodide (CuI)

Copper iodide (CuI) is employed as the hole transport layer (HTL) in the proposed trilayer perovskite solar cell due to its excellent electrical properties, wide bandgap, and high chemical stability. With a bandgap of approximately 3.1 eV, CuI exhibits high transparency within the visible spectral range, allowing incident light to reach the absorber layers without introducing significant optical losses. Furthermore, its valence band energy is well aligned with those of the perovskite absorber materials, facilitating efficient hole extraction and transport toward the rear electrode while simultaneously blocking electron backflow. Compared with conventional organic hole transport materials such as Spiro-OMeTAD, CuI offers superior chemical stability, lower fabrication cost, and simpler processing conditions. These advantages contribute to reducing interfacial recombination losses and improving charge collection efficiency. Previous numerical and experimental studies have demonstrated that the incorporation of CuI as a hole transport layer can significantly enhance photovoltaic performance and device stability, making it a suitable choice for the proposed multilayer perovskite solar cell architecture. [11,12].

2.2.7. Gold (Au)

Gold (Au) is selected as the back metal contact of the proposed trilayer perovskite solar cell owing to its high work function (5.1 ev), excellent electrical conductivity, and outstanding chemical stability. The high work function of gold promotes efficient hole collection from the CuI hole transport layer and facilitates the formation of a near-ohmic contact, thereby minimizing contact resistance and improving charge extraction efficiency. In addition, gold

exhibits strong resistance to oxidation and chemical degradation, ensuring long-term operational stability of the device. Within the proposed structure, the Au electrode serves as the final charge-collecting layer and completes the external electrical circuit, enabling the extraction of photogenerated carriers and contributing to the overall enhancement of photovoltaic performance [13,14].

2.3.SCAPS-1D Simulation Tool

2.3.1. Overview of SCAPS-1D

SCAPS-1D (Solar Cell Capacitance Simulator) is a one-dimensional numerical simulation software developed by the Department of Electronics and Information Systems at Ghent University, Belgium, for the modeling and analysis of thin-film photovoltaic devices. Owing to its accuracy, flexibility, and user-friendly interface, SCAPS-1D has become one of the most widely used simulation tools in photovoltaic research. The software enables the investigation of the electrical and optical behavior of multilayer semiconductor structures through the numerical solution of the fundamental semiconductor transport equations. It allows users to define a wide range of material parameters, including bandgap energy, electron affinity, carrier mobility, doping concentration, defect density, and interface characteristics. Furthermore, SCAPS-1D provides detailed information regarding key photovoltaic parameters such as current density–voltage (J–V) characteristics, quantum efficiency (QE), capacitance–voltage (C–V) behavior, recombination profiles, and energy band diagrams. These capabilities make it particularly suitable for studying and optimizing advanced photovoltaic structures, including multilayer and tandem perovskite solar cells, such as the trilayer configuration investigated in the present work [15].

2.3.2. Governing Physical Equations in Semiconductor Devices

The numerical calculations performed by SCAPS-1D are based on the self-consistent solution of the fundamental semiconductor equations that govern carrier transport and electrostatic behavior within photovoltaic devices. These equations include Poisson's equation, the continuity equations for electrons and holes, and the drift–diffusion transport equations. Together, these mathematical relations describe the distribution of the electric potential, carrier generation and recombination processes, and the transport of charge carriers under the influence of both electric fields and concentration gradients. By simultaneously solving these equations throughout the device structure, SCAPS-1D accurately predicts the electrical performance of solar cells and provides detailed information regarding carrier dynamics, recombination mechanisms, and photovoltaic parameters.

1. Poisson Equation

- Governs the electrostatic potential distribution inside the device.
- Relates the divergence of the electric field to the local charge density.
- Equation:

$$\nabla \cdot (\varepsilon \nabla \psi) = -q(p - n + N_D^+ - N_A^-) \quad (2.1)$$

where:

ψ: electrostatic potential

ε: permittivity

n, p: electron and hole concentrations

N_D^+, N_A^-: ionized donor and acceptor densities

2. Continuity Equations (Electrons and Holes)

- Ensure conservation of charge carriers (generation, recombination, and transport).
- Electrons:

$$\frac{\partial n}{\partial t} = \left(\frac{1}{q}\right) \nabla \cdot J_n + G_n - R_n \quad (2.2)$$

- Holes:

$$\frac{\partial p}{\partial t} = -\left(\frac{1}{q}\right) \nabla \cdot J_p + G_p - R_p \quad (2.3)$$

where:

J_n, J_p: electron and hole current densities

G: generation rate

R: recombination rate

3. Drift-Diffusion Model

- Describes carrier transport due to electric field (drift) and concentration gradient (diffusion).
- Electron current density:

$$J_n = q\,\mu_n\, n\, \nabla\psi + q\, D_n . \nabla n \quad (2.4)$$

- Hole current density:

$$J_p = -q\,\mu_p\, p\, \nabla\psi + q\, D_p\, \nabla p \quad (2.5)$$

where:

μ_n, μ_p: mobilities.

D_n, D_p: diffusion coefficients.

2.3.3. Simulation Procedure

The simulation process was performed using the SCAPS-1D software through a systematic sequence of device definition, parameter configuration, and photovoltaic characterization. Initially, the operating conditions were specified using the Action Panel interface, which serves as the main control window for executing simulations. In this interface, the working conditions, including temperature, applied voltage, frequency, and illumination settings, were defined. Standard AM1.5G solar illumination with an incident power density of 1000 W m^{-2} was employed to simulate terrestrial operating conditions. Furthermore, the Action Panel provides access to the principal simulation functions, including current density–voltage (J–V), capacitance–voltage (C–V), capacitance–frequency (C–f), and quantum efficiency (QE) analyses. The interface also allows users to configure simulation settings, define calculation procedures, and execute single or batch simulations. Figure 2.4 illustrates the SCAPS-1D Action Panel used to configure and perform the simulations.

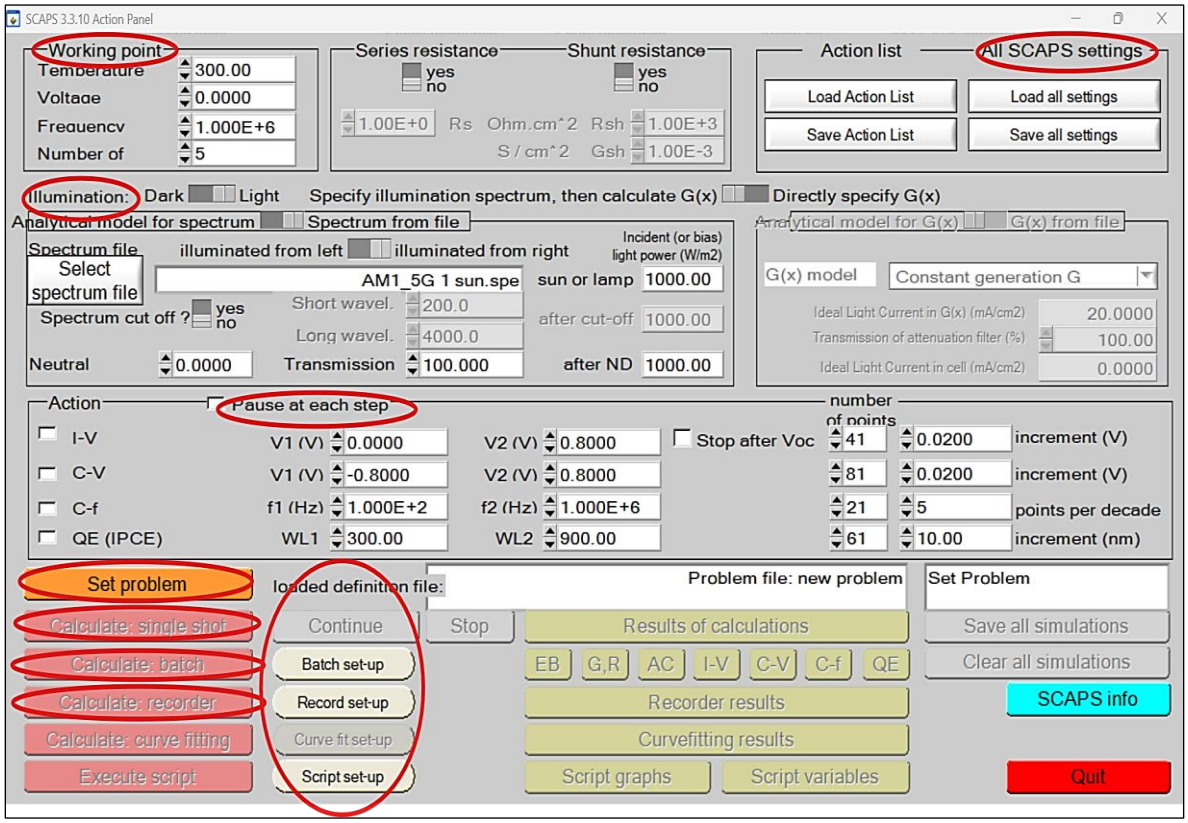

Figure 2.4: Interface for setting up and executing the simulation process

Subsequently, the device structure was established using the Cell Definition Panel, where the individual layers and interfaces of the proposed solar cell were specified. The simulated structure consisted of an ITO transparent conductive electrode, a TiO_2 electron transport layer (ETL), K_2LiAlI_6, $RbGeBr_3$, and $FA_4GeSbCl_{12}$ absorber layers, a CuI hole transport layer (HTL),

and a metallic back contact. In addition to defining the physical layers, the interfaces between adjacent materials were introduced to account for charge transport and recombination mechanisms occurring within the device. The Cell Definition Panel enables users to create, modify, save, and load device configurations while providing a graphical representation of the complete solar-cell architecture. Furthermore, the interface displays the illumination direction, current flow, voltage polarity, and layer sequence, allowing verification of the proposed configuration before performing numerical calculations. The corresponding device-definition window used in this work is shown in Figure 2.5.

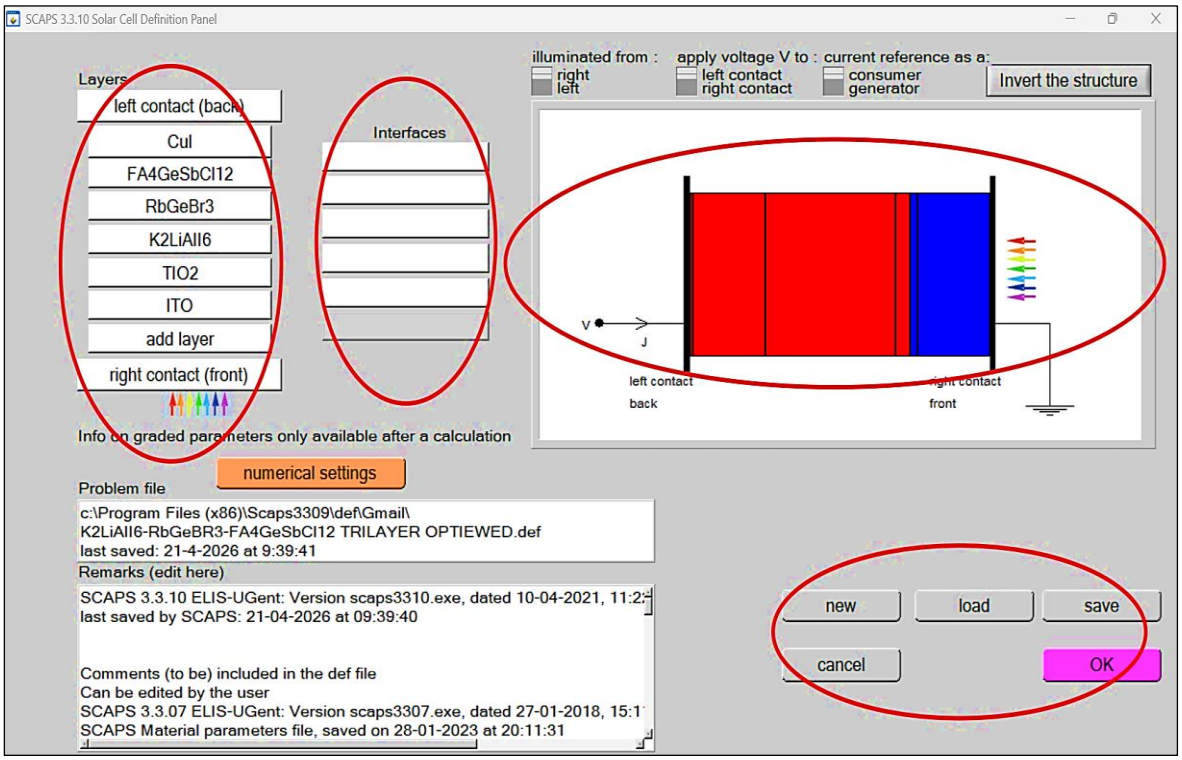

Figure 2.5: Layer selection interface

After defining the device structure, the physical and electronic properties of each layer were specified using the Layer Properties Panel in SCAPS-1D. This interface allows the user to define the fundamental material parameters, including layer thickness, bandgap energy, electron affinity, dielectric permittivity, carrier mobility, effective density of states, and doping concentrations. In addition, absorption parameters and recombination mechanisms can be introduced to accurately describe the behavior of each layer. Defect states were also incorporated where necessary to account for material imperfections and carrier recombination processes. Once all material parameters had been assigned, the photovoltaic performance of the

proposed device was evaluated through numerical simulations. Figure 2.6 shows the interface used for entering the layer properties and material parameters employed in this study. [16].

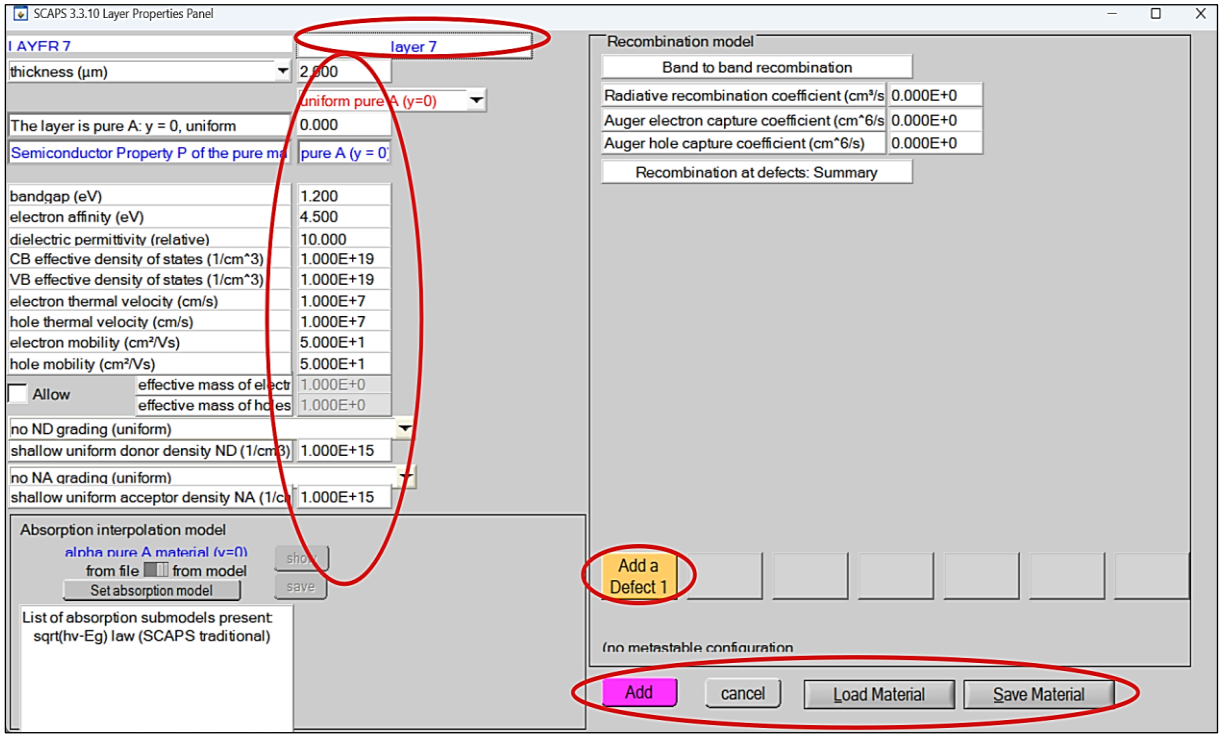

Figure 2.6: Cell layer creation interface and parameter entry.

2.4.Simulation Conditions

2.4.1. AM1.5G Illumination

All simulations are conducted under Standard Test Conditions (STC) using an AM1.5G solar spectrum, which represents global solar irradiance at Earth's surface. An incident power density of 1000 W/m² is adopted, with a irradiance spectrum that simulates natural terrestrial sunlight. These conditions are a fundamental benchmark in evaluating solar cell performance, allowing for direct comparison between simulation results and experimental results or values published in previous studies. This setup ensures the reliability and comparability of the results within the scientific research field of photovoltaics.

2.4.2. Temperature and Boundary Conditions

Operating conditions and boundary conditions are defined in the SCAPS simulation to ensure a realistic representation of the solar cell's behavior under standard conditions. In this framework, the operating temperature is set at 300 K, a standard value in most photovoltaic studies. The front electrode (ITO) is used as a transparent conductive layer that allows light

transmission while collecting charges, while the back electrode (Au) is a metallic electrode with a high work function, which contributes to improved hole extraction.

Regarding the boundary assumptions, ohmic contacts are assumed at the electrodes to ensure efficient charge carrier transfer without significant impedance, neglecting the presence of significant energy barriers at the interfaces between the layers. The simulation also relies on a steady-state assumption, assuming that the studied characteristics do not change over time during operation. These assumptions help simplify the mathematical model while maintaining acceptable accuracy in representing the actual device's behavior [17].

2.5. Conclusion

This This chapter provided an overview of the essential components and characteristics of several new and promising light-absorbing materials, with emphasis on the materials selected for our numerical study. The lead-free perovskite compounds used as light-absorbing layers—namely K_2LiAlI_6, $RbGeBr_3$, and $FA_4GeSbCl_{12}$—were thoroughly described. Additionally, other functional materials were presented, including ITO as the transparent front electrode, TiO_2 as the electron transport layer, CuI as the hole transport layer, and Au as the rear metallic contact. These materials possess favorable optoelectronic features, including strong light-harvesting capability and efficient charge carrier transport, which make them well-suited for advanced photovoltaic devices. The second part of this chapter was dedicated to the SCAPS-1D simulation package, a reliable platform for predicting and evaluating solar cell behavior. The main mathematical formulations and input variables were outlined, along with a systematic procedure for performing device simulations. This information offers the necessary background for properly analyzing simulation outputs and refining device designs to reach peak performance. Overall, the combination of material insights and simulation methodology described in this chapter lays a robust groundwork for designing and assessing high-efficiency lead-free perovskite solar cells. This foundation is crucial for the upcoming analysis and performance enhancement of device structures in the next chapter.

References chapter 02:

[1] Araújo, V. H. D., Nogueira, A. F., Tristão, J. C., & Santos, L. J. D. (2025). Advances in lead-free perovskite solar cell design via SCAPS-1D simulations. RSC Sustainability, 3, 4314–4335. https://doi.org/10.1039/D5SU00526D

[2] Zhao, Y., & Zhu, K. (2016). Organic–inorganic halide perovskites for optoelectronic applications. Chemical Society Reviews, 45(3), 655–689. https://doi.org/10.1039/C5CS00710H

[3] Granqvist, C. G. (2007). Transparent conductors as solar energy materials: A panoramic review. Solar Energy Materials and Solar Cells, 91(17), 1529–1598. https://doi.org/10.1016/j.solmat.2007.04.031

[4] Hamberg, I., & Granqvist, C. G. (1986). Evaporated Sn-doped In_2O_3 films: Basic optical properties and applications. Journal of Applied Physics, 60(11), R123–R160. https://doi.org/10.1063/1.337534

[5] Tang, H., Prasad, K., Sanjinès, R., Schmid, P. E., & Lévy, F. (1994). Electrical and optical properties of TiO_2 anatase thin films. Journal of Applied Physics, 75(4), 2042–2047.

[6] Nazeeruddin, M. K., Grätzel, M., et al. (2005). Engineering of efficient mesoscopic solar cells using TiO_2 electrodes. Science, 309(5743), 721–723.

[7] Ayyaz, A., Kaleem, M., Shakoor, A., Alkhaldi, H. D., Nasir, A., Akremi, A., Albalawi, H., & Mahmood, Q. (2025). Investigation of promising stable halide double perovskites K_2LiXI_6 (X = Al, Ga) for solar cells and thermoelectric device applications: DFT and SCAPS-1D simulation approach. Chemical Physics Letters, 879, 142433. https://doi.org/10.1016/j.cplett.2025.142433

[8] Kojima, A., Teshima, K., Shirai, Y., & Miyasaka, T. (2009). Organometal halide perovskites as visible-light sensitizers for photovoltaic cells. Journal of the American Chemical Society, 131(17), 6050–6051. https://doi.org/10.1021/ja809598r

[9] Lu, Y., Chen, X., Pan, G., Chen, Q., Chen, L., Wang, H., Wen, J., Peng, C., Li, C., & Wu, J. (2026). Numerical simulation and optimization of all inorganic $RbGeBr_3$ perovskite solar cells. Solar Energy, 303, 114119. https://doi.org/10.1016/j.solener.2025.114119

[10] Shukla, R. K., Srivastava, A., Wadhwani, N., Shukla, S., & Singh, N. (2025). Modeling and simulation of lead-free formamidinium germanium–antimony halide ($FA_4GeSbCl_{12}$) based solar cell. Journal of Optics. https://doi.org/10.1007/s12596-025-02599-6

[11] Kondrotas, R., Chen, C., & Tang, J. (2018). CuI as a hole transport material for photovoltaic applications. Solar Energy Materials and Solar Cells, 174, 144–150.

[12] Lyu, M., Yun, J. H., Cai, M., Jiao, Y., Bernhardt, P. V., Zhang, M., Wang, Q., Wang, H., & Liu, G. (2015). CuI-based hole transport layers for efficient perovskite solar cells. Advanced Energy Materials, 5(24), 1500816.

[13] Green, M. A. (1982). Solar Cells: Operating Principles, Technology and System Applications. Prentice-Hall.

[14] Sze, S. M., & Ng, K. K. (2006). Physics of Semiconductor Devices (3rd ed.). Wiley.

[15] Burgelman, M., Nollet, P., & Degrave, S. (2000). Modelling polycrystalline semiconductor solar cells. Thin Solid Films, 361–362, 527–532.

[16] Novoselov, I. E., et al. (2025). Dataset of SCAPS-1D simulated halide perovskite solar cells for photovoltaic performance analysis. Data in Brief.

[17] Burgelman, M., Decock, K., Niemegeers, A., Verschraegen, J., & Degrave, S. (2013). SCAPS Manual and User Guide. Department of Electronics and Information Systems, Ghent University, Belgium.

Chapter 3: Results and Discussion

3.1 Introduction

In this chapter, we present a detailed numerical analysis of lead-free perovskite solar cells (PSCs) using one-dimensional simulations performed with SCAPS-1D software. The study follows a progressive design strategy aimed at enhancing photovoltaic performance by broadening the spectral absorption range and maximizing power conversion efficiency. As an initial step, a single-layer absorber PSC based on K_2LiAlI_6 is simulated and analyzed, serving as a reference structure. The simulation results establish a baseline for comparing the improvements introduced by more complex architectures. To overcome the limitations of the single-absorber configuration, a second absorber layer, $RbGeBr_3$, is subsequently added, forming a bilayer PSC with the structure $K_2LiAlI_6/RbGeBr_3$. This modification is intended to extend the absorption spectrum and improve charge carrier generation. Building further upon this design, a third absorber layer, $FA_4GeSbCl_{12}$, is incorporated to create a trilayer absorbers structure denoted as $K_2LiAlI_6/RbGeBr_3/FA_4GeSbCl_{12}$. This graded-bandgap architecture enables more efficient utilization of the solar spectrum by capturing a broader range of photon energies. Following the development of the trilayer absorbers configuration, various hole transport layer (HTL) materials are investigated to identify the most suitable candidate for efficient hole extraction and minimization of recombination losses within the PSCs. A systematic parametric optimization is then performed, in which the acceptor concentration and thickness of each absorber layer (K_2LiAlI_6, $RbGeBr_3$, and $FA_4GeSbCl_{12}$) are individually varied while maintaining the previously optimized parameters for the remaining layers. This methodology allows for the determination of the optimal device configuration that yields the maximum photovoltaic performance. The simulation results are comprehensively evaluated using current density–voltage (J-V) characteristics, quantum efficiency (QE) response, and key photovoltaic parameters (open-circuit voltage, short-circuit current density, fill factor, and efficiency). These analyses provide a thorough assessment of the effectiveness of the proposed trilayer absorbers graded-bandgap architecture $K_2LiAlI_6/RbGeBr_3/FA_4GeSbCl_{12}$ in enhancing solar energy conversion efficiency for lead-free PSCs.

3.2 Device Architectures and Simulation Parameters of the Proposed PSCs

3.2.1. Structures of the Proposed PSCs

In this section, we describe the evolution of the device architecture from the reference single-layer structure to the final optimized trilayer configuration.

Stage 1: Reference single-layer structure. The starting point of this study is the reference single-layer perovskite solar cell previously proposed by *Ayyaz et al*. (2025) [1], with its structure

illustrated in Figure 3.1(a). This device is composed of ITO as the front electrode, TiO_2 as the electron transport layer (ETL), K_2LiAlI_6 as the single absorber layer, $CuAlO_2$ as the hole transport layer (HTL), and Au as the back contact. The complete reference structure can be represented as ITO/TiO_2/K_2LiAlI_6/$CuAlO_2$/Au. This configuration serves as a baseline for evaluating the improvements introduced by our proposed modifications.

Stage 2: Proposed bilayer structure. Starting from the reference configuration, we propose a first enhancement by introducing a second absorber layer, $RbGeBr_3$, to form a bilayer absorber structure. Additionally, we replace $CuAlO_2$ with CuI as the hole transport layer to improve hole extraction and reduce recombination losses. The resulting bilayer structure is denoted as ITO/TiO_2/K_2LiAlI_6/$RbGeBr_3$/CuI/Au (Figure 3.1(b)). This modification aims to broaden the spectral absorption range and enhance charge carrier generation.

Stage 3: Proposed trilayer structure. Building upon the bilayer design, we propose a further enhancement by incorporating a third absorber layer, FA4GeSbCl12, to create a trilayer absorbers configuration. The complete trilayer structure is represented as ITO/TiO_2/K_2LiAlI_6/$RbGeBr_3$/$FA_4GeSbCl_{12}$/CuI/Au, as illustrated in Figure 3.1(c). In this graded-bandgap architecture, the three absorber layers are arranged with progressively decreasing bandgap energies: the wide-bandgap K_2LiAlI_6 (top) absorbs high-energy photons, the intermediate-bandgap $RbGeBr_3$ (middle) captures visible light, and the narrow-bandgap $FA_4GeSbCl_{12}$ (bottom) harvests low-energy photons in the red and near-infrared regions. This sequential photon absorption mechanism improves light harvesting and enhances photocurrent generation.

Performance comparison and optimization. Following the development of the three architectures, a comparative analysis is performed to evaluate the photovoltaic performance of the single-layer, bilayer, and trilayer configurations. Subsequently, to further optimize the propozed perovskite solar cell, we investigate a wide range of hole transport layer (HTL) materials, including CFTS, Cu_2O, $CuCrO_2$, CuI, CuO, CuPc, CuSCN, NiO, NiO_x, P3CPenT, PEDOT:PSS, and Spiro-OMeTAD. These materials are evaluated to identify the most suitable candidate for efficient hole extraction and minimization of recombination losses. Moreover, a systematic parametric study is conducted by varying the thickness and acceptor concentration of each absorber layer (K_2LiAlI_6, $RbGeBr_3$, and $FA_4GeSbCl_{12}$) while maintaining the previously optimized parameters for the remaining layers.

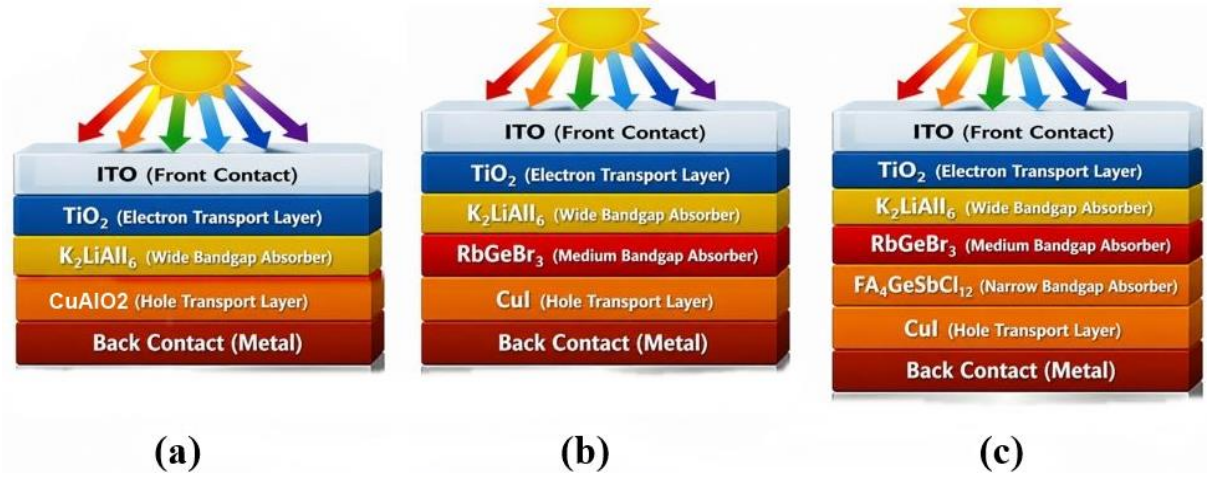

Figure 3.1: Structure of (A) Single-layer PSC, (B) Bilayer PSC, and (C) Trilayer PSC.

3.2.2. Physical Parameters Used in SCAPS-1D Simulations

The physical parameters employed in the SCAPS-1D simulations for the different layers of the proposed solar cell are summarized in Table 3.1. These parameters include layer thickness, bandgap energy, electron affinity, dielectric permittivity, carrier mobility, density of states, doping concentration, and defect density. The selected values were adopted from previously reported studies [1-4] to accurately model the electrical and optical behavior of the device, ensuring reliable simulation results and realistic performance evaluation. The simulations were performed under the AM1.5G illumination spectrum with an incident power density of 1000 W/m², and the operating temperature was set to 300 K. The back contact metal used in this study is gold (Au) with a work function of 5.1 eV [5].

Table 3.1: Physical Parameters Used in SCAPS-1D Simulations [1-4].

Layers / Parameters	ITO	TIO_2	K_2LiAlI_6	$RbGeBr_3$	$FA_4GeSbCl_{12}$	$CuAlO_2$	CuI
Thickness, t_m (nm)	500	50	800	500	500	20	20
Bandgap, E_g (eV)	3.5	3.2	1.73	1.49	1.30	3.46	3.1
Electron affinity, χ_e (eV)	4	4	4.07	3.8	3.5	2.5	2.1
Dielectric ratio, E_{ps}	9	9	3.53	7	2.59	60	6.5
Electron mobility, μ_n (cm^2/Vs)	20	2×10^{1}	1.5×10^{-1}	160	2268	2	100
Hole mobility, μ_p (cm^2/Vs)	10	1×10^{1}	2.8×10^{-2}	160	478	8.6	43.9
Valence band density of states, N_v (cm^{-3})	1.8×10^{19}	1.8×10^{19}	1.2×10^{19}	1×10^{15}	2.0×10^{18}	1.8×10^{19}	1×10^{19}
Conduction band density of states, N_c (cm^{-3})	2×10^{19}	2×10^{19}	9.2×10^{17}	1×10^{16}	2.2×10^{18}	2.2×10^{18}	2.8×10^{19}

Donor concentration, N_d (cm^{-3})	1×10^{21}	1×10^{16}	0	0	0	0	0
Acceptor concentration, N_a (cm^{-3})	0	0	1×10^{17}	2×10^{13}	1.0×10^{20}	1×10^{18}	1×10^{18}
Defect Density, N_t (cm^{-3})	1×10^{15}	1×10^{14}	1×10^{14}	1×10^{17}	1.0×10^{16}	1×10^{14}	1×10^{15}

3.3 Simulation results

3.3.1. Comparison Validation and Comparison of Single, Bilayer, and Trilayer Structures

In this subsection, we present the validation of our simulation model along with a comparative performance analysis of the three proposed device architectures. The investigation started with a single-junction PSC employing K_2LiAlI_6 as the sole absorber layer. Subsequently, a bilayer design was developed by adding $RbGeBr_3$ as a second absorber layer. Finally, a trilayer architecture was constructed by incorporating $FA_4GeSbCl_{12}$ as a third absorber layer. These three configurations are schematically illustrated in Figure 3.1.

The comparative simulation results for the single-junction, bilayer, and trilayer PSCs are displayed in Figures 3.2 and 3.3. The current–voltage (J–V) characteristics of the single-junction K_2LiAlI_6-based device yielded a power conversion efficiency (PCE) of 21.79%. A comparison between our simulated results presented in Table 3.1 and the numerical data previously reported by Ayyaz et al. (2025) [1] shows good agreement, thereby validating the accuracy of our SCAPS-1D simulation approach.

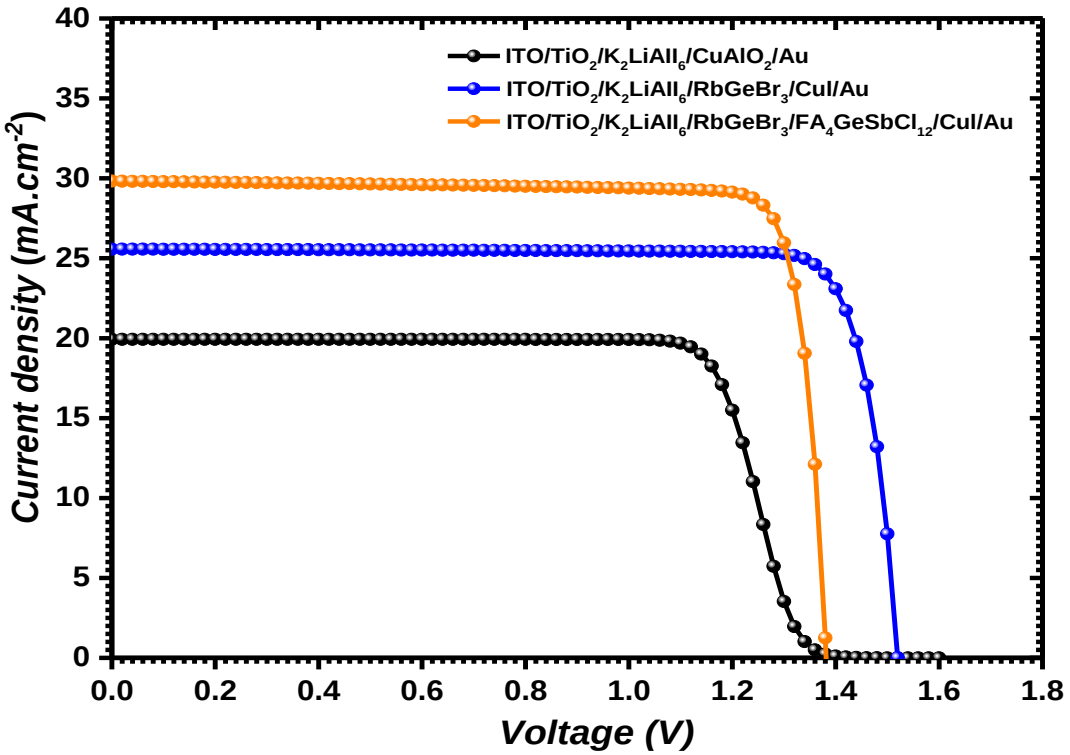

Figure 3.2: J–V Characteristics of the Single-Layer (K_2LiAlI_6), Bilayer (K_2LiAlI_6/$RbGeBr_3$), and Trilayer (K_2LiAlI_6/$RbGeBr_3$/$FA_4GeSbCl_{12}$) PSCs.

The introduction of the $RbGeBr_3$ absorber layer with CuI as the HTL resulted in a significant enhancement in device performance, with the short-circuit current density (J_{sc}) increasing from 19.93 mA cm^{-2} to 25.57 mA cm^{-2} and the fill factor (FF) improving from 68.15% to 86.21%, leading to a remarkable increase in efficiency to 33.51%. This improvement is primarily attributed to the expanded absorption range and the enhanced generation and collection of photogenerated charge carriers. Further enhancement was achieved by incorporating the $FA_4GeSbCl_{12}$ absorber layer, which increased the short-circuit current density to 29.82 mA cm^{-2} and raised the efficiency to 35.75%. Despite a further slight decrease in open-circuit voltage (V_oc), the continued increase in J_sc contributed to the overall performance improvement. The observed progressive improvement from the single-layer to the bilayer and subsequently to the trilayer structure demonstrates the effectiveness of the graded-bandgap absorber configuration in extending spectral absorption, increasing carrier generation, and improving overall photovoltaic performance.

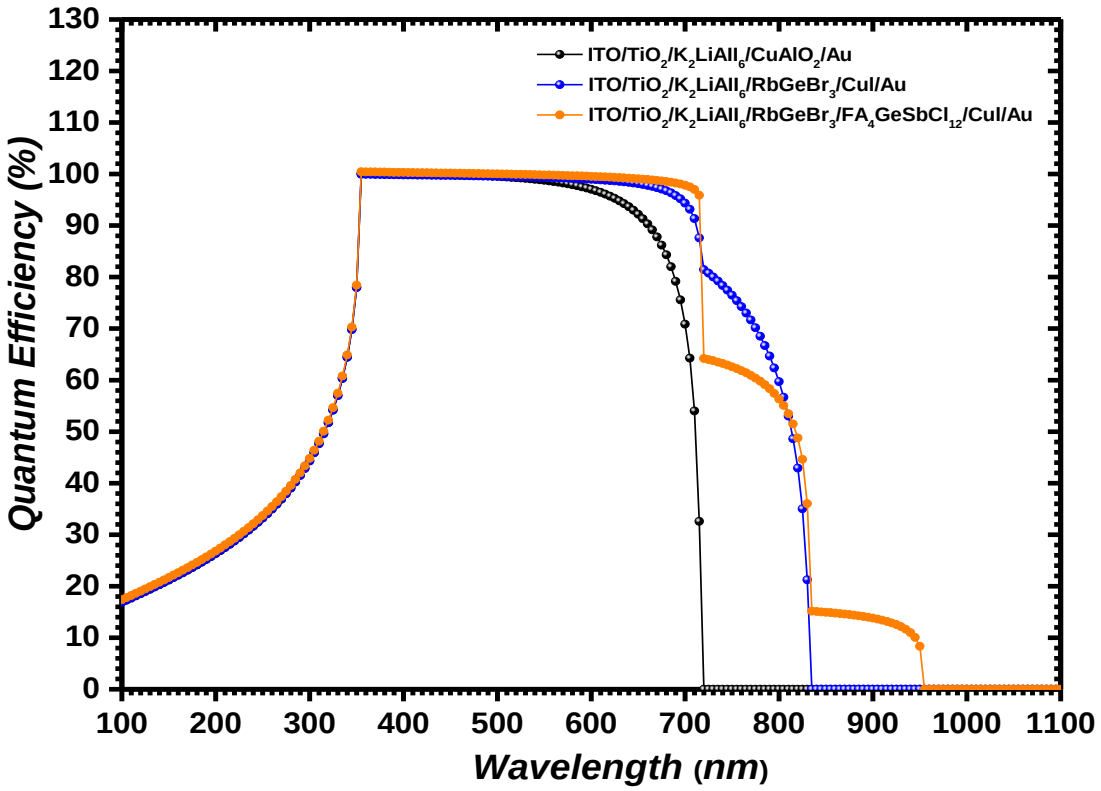

Figure 3.3: QE versus Wavelength for Single-Layer (K_2LiAlI_6), Bilayer ($K_2LiAlI_6/RbGeBr_3$), and Trilayer ($K_2LiAlI_6/RbGeBr_3/FA_4GeSbCl_{12}$) PSCs.

This progressive enhancement is clearly illustrated in Figures 3.2 and 3.3. Figure 3.2 displays the current density–voltage (J–V) characteristics of the three configurations, where a clear shift toward higher current densities and improved fill factors is observed as additional absorber layers are introduced, even though the open-circuit voltage shows a slight decline. The single-layer

device (K_2LiAlI_6) exhibits the lowest J_{sc} and PCE, while the bilayer ($K_2LiAlI_6/RbGeBr_3$) and trilayer ($K_2LiAlI_6/RbGeBr_3/FA_4GeSbCl_{12}$) devices show progressively enhanced performance. Similarly, Figure 3.3 presents the quantum efficiency (QE) spectra of the three devices, indicating enhanced utilization of the solar spectrum and increased photogenerated carrier generation. While the single-layer device exhibits a strong response mainly below 720 nm, the incorporation of $RbGeBr_3$ extends the photoresponse to approximately 850 nm, and the addition of $FA_4GeSbCl_{12}$ further broadens it into the near-infrared region beyond 950 nm. The trilayer structure demonstrates a broader spectral response extending further into the near-infrared region compared to the bilayer and single-layer configurations, confirming improved photon harvesting across a wider range of wavelengths. This broadening of the QE spectrum directly correlates with the observed increase in J_{sc} and overall efficiency, despite the slight reduction in V_{oc}. The results clearly indicate that the integration of multiple absorber layers with complementary bandgaps provides a highly effective strategy for maximizing solar spectrum utilization and enhancing energy conversion efficiency [1,5].

Table 3.2: Performance Comparison of the Simulated Devices

Device configuration	J_{sc} (mA/cm^2)	V_{oc} (V)	*FF* (%)	*PCE* (%)
ITO/TiO2/K2LiAlI6/CuAlO2/au (2025) [1]	19.72	1.35	82.28	22.05
ITO/TiO2/K2LiAlI6/ CuAlO2/au (This work)	19.93	1.60	68.15	21.79
ΙΟ/TiO2/K2LiAlI6/RbGeBr3/CuI/au (This work)	25.57	1.52	86.21	33.51
ITO/TiO2/K2LiAlI6/RbGeBr3/FA4GeSbCl12/CuI/au (This work)	29.83	1.38	86.74	35.75

3.4 Optimization of Trilayer ($K_2LiAlI_6/RbGeBr_3/FA_4GeSbCl_{12}$) PSC

In this section, after proving the effectiveness of the trilayer architecture, we introduce optimization strategies for the Trilayer ($K_2LiAlI_6/RbGeBr_3/FA_4GeSbCl_{12}$) PSC to enhance its overall performance. A systematic parametric study is conducted to identify the optimal conditions that maximize power conversion efficiency. The optimization process includes the following key aspects:

- Investigation of various hole transport layer (HTL) materials to determine the most suitable candidate for efficient hole extraction and minimization of recombination losses.
- Optimization of absorber layer thicknesses for K_2LiAlI_6, $RbGeBr_3$, and $FA_4GeSbCl_{12}$ to achieve balanced carrier generation and collection.

- Optimization of acceptor concentrations for each absorber layer to enhance the built-in potential and improve charge transport.

The following subsections present a detailed analysis of each optimization parameter, leading to the identification of the optimal device configuration for the proposed trilayer lead-free perovskite solar cell.

3.4.1. Selection of the Optimal Hole Transport Layer HTL

The The hole transport layer (HTL) plays a crucial role in determining the performance of perovskite solar cells by facilitating hole extraction and minimizing charge recombination at the interface between the absorber material and the HTL [6,9]. To identify the most suitable HTL for the proposed trilayer architecture, we screened several organic and inorganic hole transport materials using SCAPS-1D software. The comparison was based on key photovoltaic performance parameters, including short-circuit current density (J_sc), open-circuit voltage (V_oc), fill factor (FF), and power conversion efficiency (PCE).

In this analysis, eleven different HTL materials were investigated and compared. These include CFTS, Cu_2O, CuI, CuO, NiO, Spiro-OMeTAD, P3CPenT, CuPc, $CuCrO_2$, CuSCN and PEDOT:PSS. The material parameters used for each HTL in the numerical simulations are listed in Table 3.3, and the corresponding results are presented in Table 3.4.

Table 3.3: Physical Parameters of the Investigated HTLs [2,3,6-10].

Parameters	CFTS	Cu_2O	CuI [6]	$CuCrO_2$	CuSCN	Spiro-OmeTAD	P3CPenT	PEDOT :PSS
E_g (eV)	1.300	2.170	3.100	3	3.4	2.88	2.070	1.8
χ_e (eV)	3.300	3.200	2.1	2.1	1.7	2.05	3.090	3.5
E_{ps}	9.000	7.500	3	9.5	10	3	7.6	10
μ_n (cm^2/Vs)	21.98	20	100	0.1	2×10^{-4}	2×10^{-4}	3.2×10^{-4}	1×10^{-2}
μ_p (cm^2/Vs)	21.98	80	43.9	2.53	2×10^{-1}	2×10^{-4}	3.9×10^{-4}	8×10^{-1}
N_v (cm^{-3})	1.8×10^{19}	1.8×10^{18}	1.0×10^{19}	1×10^{19}	2.5×10^{21}	1.8×10^{19}	2.5×10^{20}	1.8×10^{19}
N_c (cm^{-3})	2.2×10^{18}	2×10^{18}	2.8×10^{19}	1×10^{19}	1.7×10^{19}	2.2×10^{18}	2.5×10^{20}	2.2×10^{18}
N_d (cm^{-3})	-	-	-	-	-	-	-	-
N_a (cm^{-3})	1×10^{16}	1×10^{15}	1×10^{18}	1×10^{18}	1×10^{18}	1×10^{18}	1×10^{18}	1×10^{18}
N_t (cm^{-3})	1×10^{15}	1×10^{14}	1.0×10^{15}	1×10^{15}	1×10^{15}	2.2×10^{15}	1×10^{15}	1×10^{15}

The results indicate that most hole transport layers provide relatively similar values for short-circuit current density (J_sc) and open-circuit voltage (V_oc), while significant differences were observed in the fill factor (FF) and overall conversion efficiency (PCE). Among the materials

studied, copper iodide (CuI) achieved one of the highest efficiencies, at 35.75%, along with a high fill factor of 86.74%. This outstanding performance is attributed to the compatibility of its energy levels with the absorber layers, which facilitates efficient hole extraction while inhibiting electron recombination at the interface. In addition, CuI possesses good hole mobility and excellent chemical stability, making it a suitable candidate for high-performance perovskite solar cells. Although some materials such as copper chromium oxide ($CuCrO_2$) and copper thiocyanate (CuSCN) showed comparable efficiencies, CuI was selected for subsequent optimization studies due to its balanced electrical performance, compatibility with the device structure, and promising stability properties [2].

Table 3.4: Electrical Performance Comparison of Various HTLs in the $K_2LiAlI_6/RbGeBr_3/FA_4GeSbCl_{12}$ Trilayer PSC.

HTLs	Jsc (mA/cm2)	Voc(V)	FF (%)	PCE (%)
CFTS	29.11	1.37	86.46	34.66
Cu_2O	29.82	1.38	85.75	35.34
CuI	29.82	1.38	86.74	35.75
CuO	29.82	1.38	86.40	35.61
CuPc	29.82	1.38	86.73	35.74
CuSCN	29.82	1.38	86.74	35.75
NiO	29.78	1.38	80.94	33.32
P3CPenT	29.82	1.38	86.46	35.63
$CuCrO_2$	29.82	1.38	86.74	35.75
PEDOT:PSS	29.55	1.37	86.48	35.20
Spiro-OmeTAD	29.82	1.38	86.58	35.68

Following the selection of the optimal hole transport layer, the optimization of the trilayer solar cell was initiated by investigating the K_2LiAlI_6 top absorber layer. The optimization process focused on two key parameters, namely the acceptor concentration (N_a) and the absorber thickness, due to their significant influence on charge transport, carrier recombination, and overall device performance. Initially, the acceptor density was varied while maintaining all other device parameters constant in order to determine the optimum doping concentration corresponding to the maximum power conversion efficiency. Once the optimum acceptor concentration was identified, it was fixed for the subsequent optimization step, and the absorber thickness was varied to determine the optimum value that provides the best balance between photon absorption, charge collection, and recombination losses.

3.4.2. Optimization of the Acceptor Density (N_a) and Top Absorber (K_2LiAlI_6) Layer Thickness

To determine the optimal acceptor concentration (N_a) for the K_2LiAlI_6 top absorber layer, a parametric study was performed by varying the doping density from 10^11 cm^{-3} to 10^{20} cm^{-3} while keeping all other device parameters constant. The corresponding photovoltaic results and power conversion efficiency (PCE) were recorded for each value, as presented in Figure 3.4. The results show that the energy conversion efficiency increases gradually with increasing acceptor density until it reaches an optimum value of approximately 35.75% at 10^{17} cm^{-3}, after which it decreases with further increasing doping. At low doping concentrations, the limited density of free holes leads to poor electrical conductivity and charge transport, as well as increased recombination losses. With increasing acceptor density, the internal electric field becomes stronger, improving charge separation, enhancing hole transport, and reducing charge recombination. Consequently, the photovoltaic cell parameters improve, particularly the open-circuit voltage (V_oc) and fill factor (FF), resulting in higher conversion efficiency. However, exceeding the optimum doping concentration leads to decreased efficiency due to the formation of defects and additional recombination centers, which increases charge losses and reduces charge mobility. Therefore, an acceptor density of 10^{17} cm^{-3} provides the optimal balance between improving conductivity and minimizing recombination losses in the top absorber layer K_2LiAlI_6. Thus, we maintain the initial doping concentration at 10^{17} cm^{-3} for subsequent optimization steps.

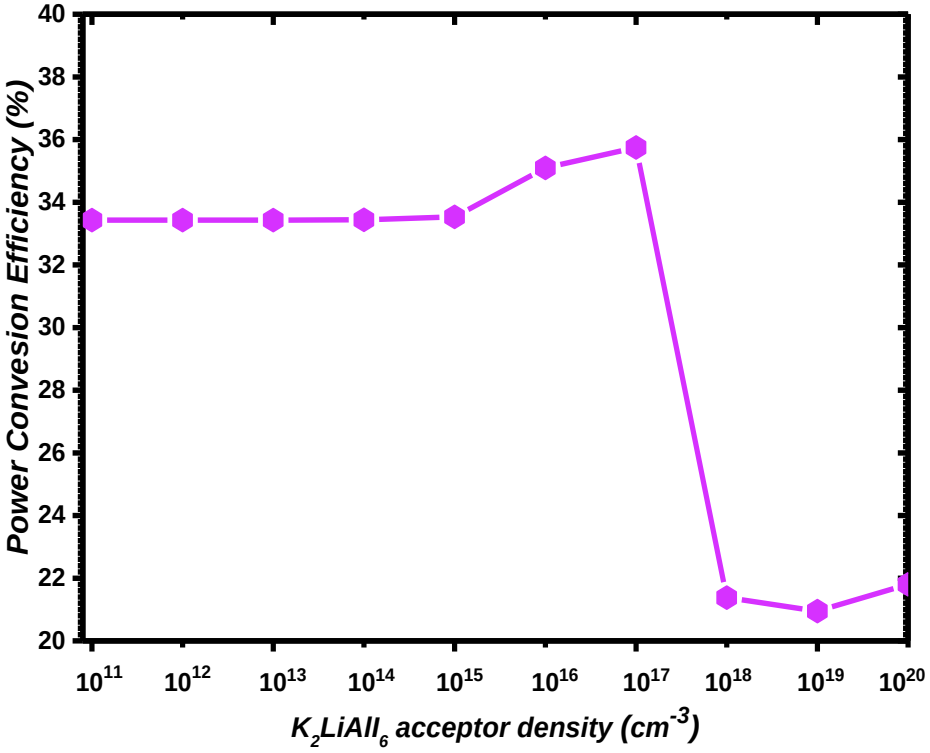

Figure 3.4: PCE as a Function of Acceptor Density (N_a) for the K_2LiAlI_6 Top Absorber Layer in the Trilayer PSC.

After determining the optimum acceptor concentration in the K_2LiAlI_6 absorber layer, the influence of absorber thickness on the photovoltaic performance was then investigated to determine the optimum thickness that provides the best balance between photon absorption, charge transport, and recombination losses. The effect of the K_2LiAlI_6 absorber thickness on device performance is presented in Figure 3.5. The results indicate that the highest power conversion efficiency, approximately 40.32%, is achieved at a thickness of about 100 nm. Beyond this optimal value, the PCE gradually declines with increasing thickness across the entire range from 100 nm to 1200 nm, reaching a PCE of 33.41% at 1200 nm. This behavior can be attributed to the wide bandgap and high absorption coefficient of K_2LiAlI_6, which enable efficient absorption of high-energy photons near the surface region of the layer. At lower thicknesses (around 100 nm), photogenerated carriers travel shorter distances before reaching the transport layers, thereby reducing recombination losses and improving charge collection. However, increasing the absorber thickness beyond the optimum value leads to a gradual decline in efficiency due to increased carrier transport distance, higher recombination probability, and greater resistive losses. Therefore, a relatively thin K_2LiAlI_6 layer provides the best compromise between efficient photon absorption and effective charge extraction. Thus, we fixed the thickness at 100 nm. In addition, this behavior is consistent with previous results in the literature, such as [11].

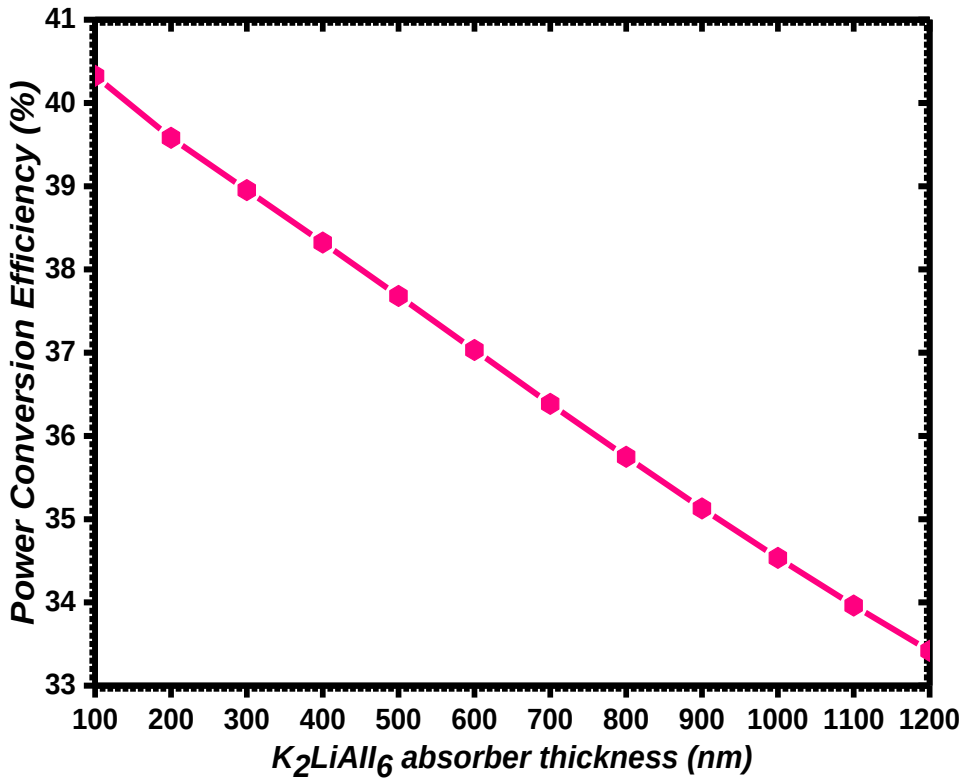

Figure 3.5: PCE as a Function of Thickness (t_m) for the K_2LiAlI_6 Top Absorber Layer in the Trilayer PSC.

3.4.3. Optimization of the Acceptor Density (N_a) and Middle Absorber ($RbGeBr_3$) Layer Thickness

After optimizing the top absorber layer (K_2LiAlI_6) with a fixed acceptor density of 10^{17} cm^{-3} and thickness of 100 nm, we proceed to optimize the middle absorber layer ($RbGeBr_3$) using the same approach by varying the $RbGeBr_3$ doping density from 10^{11} cm^{-3} to 10^{20} cm^{-3} while keeping all other device parameters constant. The influence of acceptor density on the photovoltaic performance of the $RbGeBr_3$ middle absorber layer is illustrated in Figure 3.6.

As manifested, at lower doping concentrations, the efficiency remains nearly constant because the carrier density is already sufficient to maintain adequate charge transport and separation within this range, with no significant recombination losses. However, when the doping concentration exceeds the optimum value, the efficiency gradually decreases due to the formation of additional defects and recombination centers associated with excessive impurity incorporation, which negatively affects carrier transport and increases recombination losses.

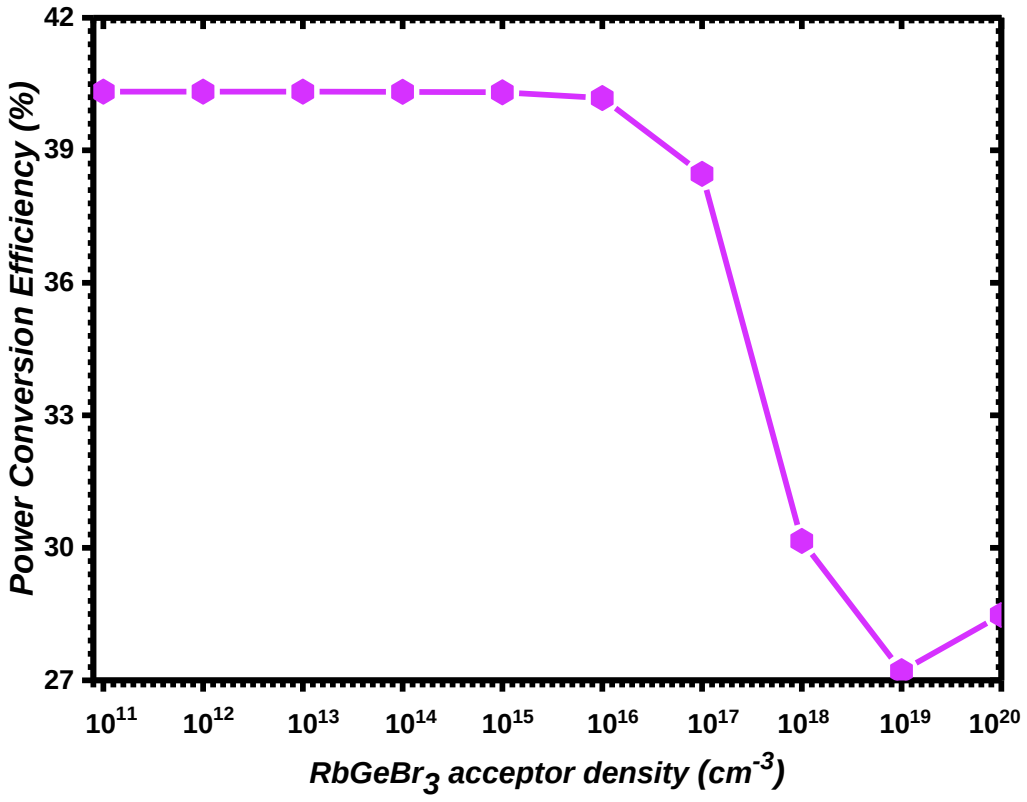

Figure 3.6: PCE as a Function of Acceptor Density (N_a) for the $RbGeBr_3$ Middle Absorber Layer in the Trilayer PSC.

After fixing the acceptor concentration for the $RbGeBr_3$ middle absorber layer at 2×10^{13} cm^{-3}, the thickness was varied from 100 nm to 1200 nm while keeping all previously optimized parameters constant. The results presented in Figure 3.7 show that the power conversion efficiency increases slightly with increasing thickness, from approximately 39.5% at 100 nm to a maximum value of

about 40.43% at 800 nm, after which it saturates. However, given that the efficiency values across the thickness range from 500 nm to 1200 nm are very close, with differences of less than 0.1%, the improvement beyond 500 nm is considered marginal. Therefore, to maintain a reasonably thin absorber layer and avoid unnecessary material usage without compromising device performance, we chose to keep the initial thickness of the $RbGeBr_3$ layer at 500 nm for subsequent optimization steps. This slight improvement is attributed to the increased thickness providing a sufficient optical path length to absorb the majority of photons within the spectral range of the $RbGeBr_3$ layer. Beyond 800 nm, the absorber becomes optically saturated, where further thickness increase does not yield additional photon absorption or efficiency gain.

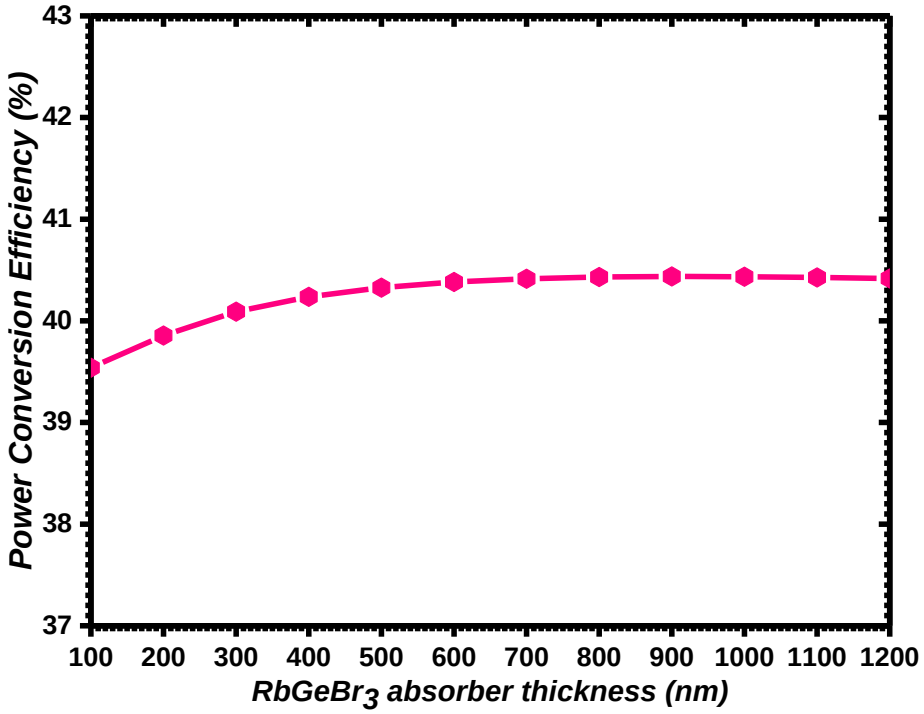

Figure 3.7: PCE as a Function of Thickness (t_m) for the $RbGeBr_3$ Middle Absorber Layer in the Trilayer PSC.

3.4.4. Optimization of the Acceptor Density (N_a) and Bottom Absorber ($FA_4GeSbCl_{12}$) Layer Thickness

Having established the optimal parameters for the top (K_2LiAlI_6) and middle ($RbGeBr_3$) absorber layers, we subsequently investigated the influence of the bottom absorber layer ($FA_4GeSbCl_{12}$) on the performance of the trilayer PSC. The influence of acceptor density on the photovoltaic performance of the $FA_4GeSbCl_{12}$ bottom absorber layer is presented in Figure 3.8. The acceptor concentration was varied from 10^{11} cm^{-3} to 10^{20} cm^{-3} while keeping all other parameters constant. The results indicate that the power conversion efficiency remains relatively stable at lower doping concentrations up to 10^{16} cm^{-3}, then begins to increase significantly starting from 10^{17} cm^{-3} and reaches a maximum value of approximately 40.33% at an acceptor density of

10^{20} cm^{-3}. At low doping levels, the carrier concentration within the absorber layer is insufficient for efficient charge extraction, leading to poor electrical conductivity and increased recombination losses. As the acceptor density increases, the built-in electric field becomes stronger, promoting more effective separation of photogenerated carriers, improving hole extraction, reducing carrier accumulation at the interfaces, and enhancing the electrical conductivity of the absorber layer. These effects contribute to improvements in the open-circuit voltage (V_{oc}), short-circuit current density (J_{sc}), and fill factor (FF), resulting in enhanced power conversion efficiency. Thus, we adopt the optimal doping concentration of 10^{20} cm^{-3} for the $FA_4GeSbCl_{12}$ bottom absorber layer for subsequent optimization steps. It should be noted that higher doping concentrations beyond 10^{20} cm^{-3} were not investigated, as further increasing the doping level may cause the semiconductor to exhibit metallic behavior, which could adversely affect device performance.

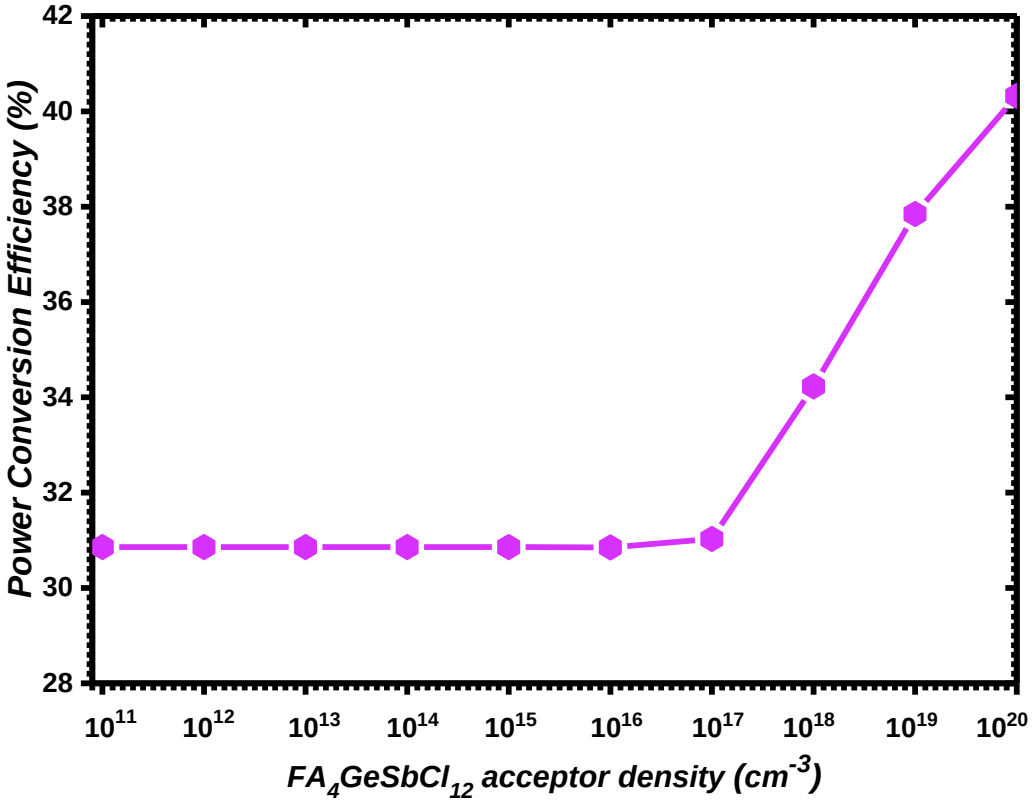

Figure 3.8: PCE as a Function of Acceptor Density (N_a) for the $FA_4GeSbCl_{12}$ Bottom Absorber Layer in the Trilayer PSC.

Finally, Figure 3.9 illustrates the effect of the thickness of the $FA_4GeSbCl_{12}$ bottom absorber layer on the photovoltaic performance of the proposed solar cell. The results indicate that the energy conversion efficiency increases with increasing absorber thickness, reaching a maximum value of about 40.88% at a thickness of approximately 800 nm, after which it shows a very slight decline or saturation. This remarkable increase in efficiency is mainly attributed to the enhanced

absorption of low-energy photons and the resulting increase in the number of photogenerated charge carriers. With increasing thickness, the optical path length within the absorber layer increases, allowing for the absorption of a larger proportion of the incident solar radiation and contributing to an improved short-circuit current density (J_{sc}). This behavior is crucial for the $FA_4GeSbCl_{12}$ layer, which is responsible for absorbing photons in the red and near-infrared regions of the solar spectrum, thereby contributing substantially to the overall enhancement of device performance. Consequently, a thickness of 800 nm was selected for the $FA_4GeSbCl_{12}$ bottom absorber layer, as it provides adequate optical absorption across its characteristic spectral range.

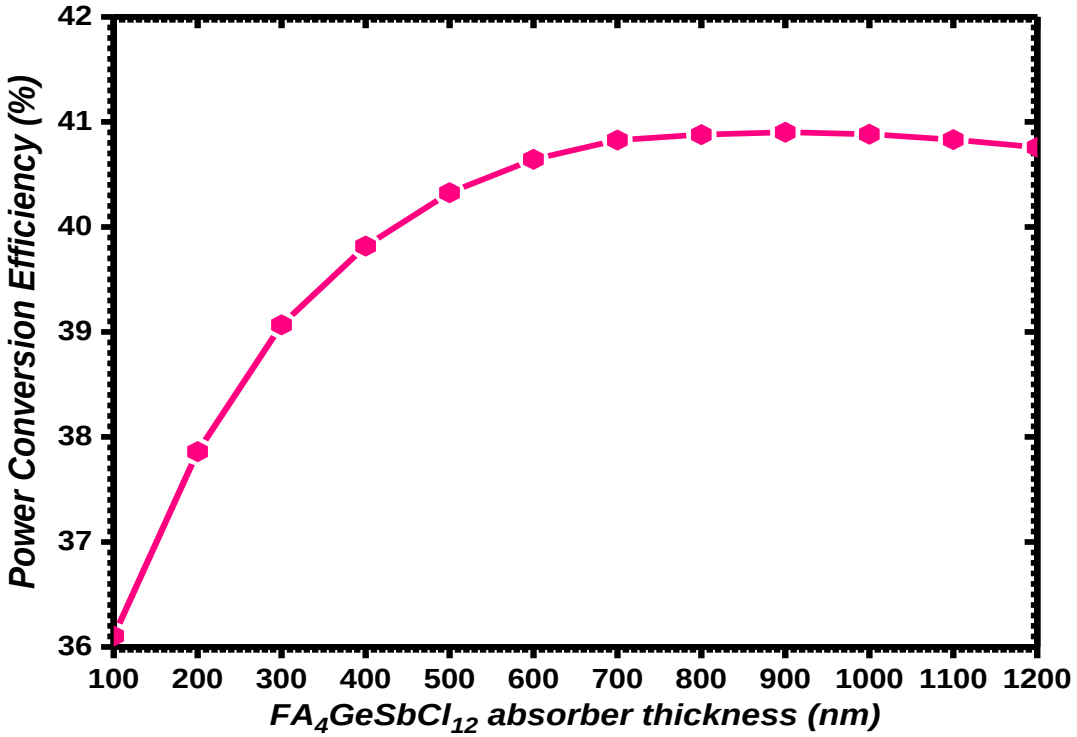

Figure 3.9: PCE as a Function of Thickness (t_m) for the $FA_4GeSbCl_{12}$ Bottom Absorber Layer in the Trilayer PSC.

3.5 Final Optimized Device

3.5.1. Optimal Device Configuration

Following the systematic parametric optimization presented in the preceding sections, the final optimal device configuration was established. The optimized trilayer PSC comprises a K_2LiAlI_6 top absorber layer (thickness: 100 nm, acceptor concentration: 1×10^{17} cm^{-3}), an $RbGeBr_3$ middle absorber layer (thickness: 500 nm, acceptor concentration: 2×10^{13} cm^{-3}), and a $FA_4GeSbCl_{12}$ bottom absorber layer (thickness: 800 nm, acceptor concentration: 1×10^{20} cm^{-3}),

with CuI serving as the optimal hole transport layer (HTL). The complete architecture of the optimized trilayer absorber is depicted in Figure 3.10.

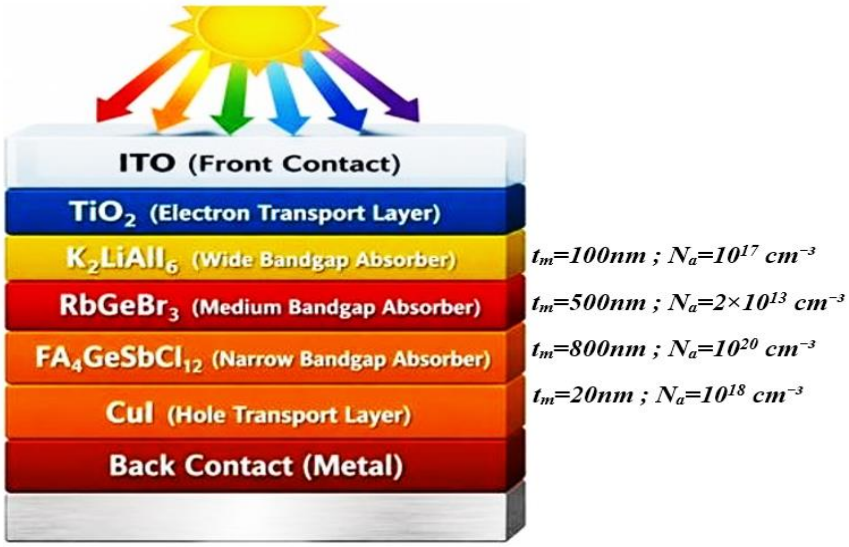

Figure 3.10: Optimal Device Configuration of the Trilayer Absorber PSC.

3.5.2. Performance Comparison Between Optimized Trilayer and Previous Configurations

The photovoltaic performance of the optimized configuration was evaluated and compared with the initial devices through quantum efficiency (QE) and current density–voltage (J–V) analyses. Figure 3.11 presents the current density–voltage (J–V) characteristics of the single-layer, bilayer, initial trilayer, and optimized trilayer solar cell structures. The results clearly demonstrate a gradual improvement in photovoltaic performance with the addition of absorber layers and the optimization of device parameters. The short-circuit current density (J_{sc}) increases from 19.93 mA/cm² for the single-layer device to 25.57 mA/cm² for the bilayer structure, then to 29.82 mA/cm² for the initial trilayer structure, reaching a maximum value of 33.47 mA/cm² after optimization. It is worth noting that although the open-circuit voltage (V_{oc}) decreases progressively from 1.60 V for the single-layer device to 1.52 V, 1.38 V, and finally 1.37 V for the optimized trilayer structure, the substantial increase in J_{sc} and FF more than compensates for this reduction, resulting in a net gain in overall efficiency. This improvement is primarily attributed to the broader spectral absorption achieved by integrating absorber layers with different bandgap energies, allowing for more efficient utilization of high, medium, and low-energy photons, in addition to the suitable parameters of thickness and doping.

Table 3.5 summarizes the characteristics extracted from the J–V curves for all studied structures. Furthermore, the optimized device exhibits an enhanced fill factor (FF) of 88.67%, indicating more efficient charge transfer and reduced recombination losses within the device. Consequently, the power conversion efficiency (PCE) increased significantly from 21.79% for

the single-absorber reference structure to 40.88% for the optimized trilayer solar cell. These results confirm the effectiveness of the proposed graded-bandgap design and highlight the importance of optimizing the absorber layers in achieving high photovoltaic performance.

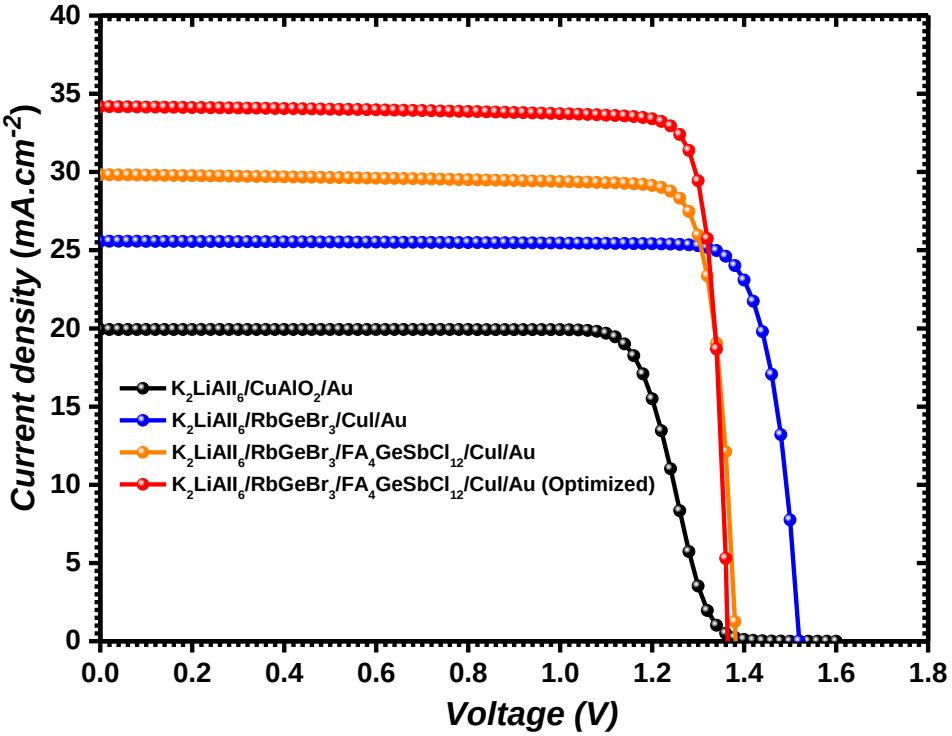

Figure 3.11: Comparison of J–V Characteristics for Single, Bilayer, Initial Trilayer, and Optimized Trilayer PSCs.

For more detail, Figure 3.12 presents the quantum efficiency (QE) spectra of the single-layer, bilayer, initial trilayer, and optimized trilayer solar cells. The results clearly demonstrate that the optimized trilayer device exhibits the highest quantum efficiency over the widest wavelength range compared to the other device configurations. This enhancement reflects more effective utilization of the solar spectrum and a greater capability for photon harvesting and charge carrier collection. The improvement can be attributed to the optimized absorber thicknesses and acceptor concentrations, which enhance light absorption and reduce carrier recombination losses. Furthermore, the combination of K_2LiAlI_6, $RbGeBr_3$, and $FA_4GeSbCl_{12}$ absorber layers forms a graded-bandgap architecture that enables efficient absorption of high, medium, and low-energy photons across different regions of the solar spectrum. Consequently, a larger fraction of incident photons contributes to photocurrent generation, resulting in enhanced photovoltaic performance and confirming the effectiveness of the proposed optimized trilayer design.

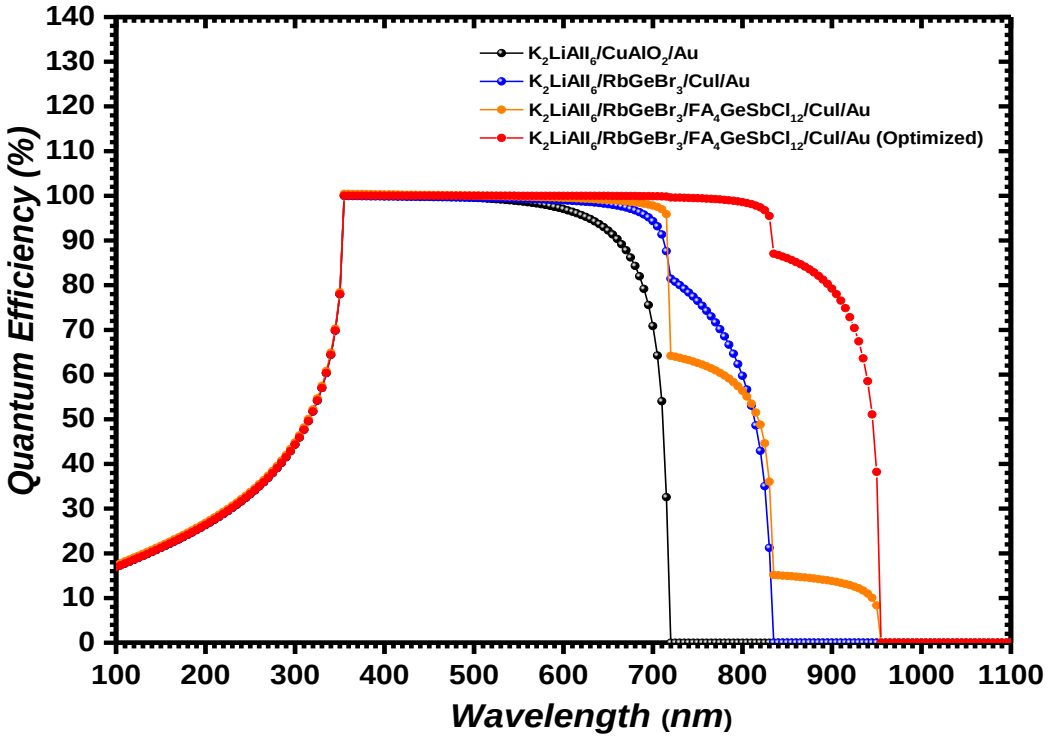

Figure 3.12: Comparison of QE Characteristics for Single, Bilayer, Initial Trilayer, and Optimized Trilayer PSCs.

Table 3.5: Evolution of Photovoltaic Performance with Successive Device Optimization.

Device configuration	J_{sc} (mA/cm^2)	V_{oc}(V)	*FF* (%)	*PCE* (%)
ITO/TiO2/K2LiAlI6/CuAlO2/au [3] (2025)	19.72	1.35	82.28	22.05
ITO/TiO2/K2LiAlI6/ CuAlO2/au (This work)	19.93	1.60	68.15	21.79
ITO/TiO2/K2LiAlI6/RbGeBr3/CuI/au (This work)	25.57	1.52	86.21	33.51
ITO/TiO2/K2LiAlI6/RbGeBr3/FA4GeSbCl12/CuI/au (This work)	29.82	1.38	86.74	35.75
ITO/TiO2/K2LiAlI6/RbGeBr3/FA4GeSbCl12/CuI/au (optimized) (This work)	34.18	1.37	87.62	40.88

3.6 Conclusion

This chapter presented a comprehensive numerical investigation and optimization of lead-free perovskite solar cells (PSCs) using one-dimensional simulations performed with SCAPS-1D software. The study began with the simulation of a single-layer K_2LiAlI_6-based solar cell, which served as the reference structure for subsequent analyses. A comparison between our simulated results and the numerical data previously reported by Ayyaz et al. (2025) showed good agreement, thereby validating the accuracy of our simulation approach. Recognizing the limitations in efficiency of the single-absorber structure, we proposed a bilayer configuration by incorporating

$RbGeBr_3$ as a second absorber layer with CuI as the hole transport layer (HTL), resulting in the stacked bilayer structure ITO/TiO_2/K_2LiAlI_6/$RbGeBr_3$/CuI/Au. Comparative analysis clearly demonstrated the performance enhancement offered by the bilayer design, particularly in terms of improved light absorption and charge collection. Further improvement was achieved by introducing $FA_4GeSbCl_{12}$ as a third absorber layer, creating a trilayer architecture (K_2LiAlI_6/$RbGeBr_3$/$FA_4GeSbCl_{12}$) capable of utilizing a broader portion of the solar spectrum.

To further enhance device performance, we undertook a systematic optimization of key parameters. A comparative evaluation of eleven different hole transport materials identified CuI as the most suitable HTL for the proposed device, achieving an efficiency of 35.75% with a high fill factor of 86.74%. Subsequently, a systematic parametric optimization was performed by varying the acceptor concentration and thickness of each absorber layer. The optimal parameters were determined as follows: for the K_2LiAlI_6 top absorber layer, a thickness of 100 nm and acceptor concentration of 1×10^{17} cm^{-3}; for the $RbGeBr_3$ middle absorber layer, a thickness of 500 nm and acceptor concentration of 2×10^{13} cm^{-3}; and for the $FA_4GeSbCl_{12}$ bottom absorber layer, a thickness of 800 nm and acceptor concentration of 1×10^{20} cm^{-3}. The results demonstrated that the optimized trilayer structure exhibited superior photovoltaic performance compared with the reference and intermediate configurations. It is worth noting that although the open-circuit voltage (V_{oc}) decreased progressively from 1.60 V for the single-layer device to 1.37 V for the optimized trilayer structure, the substantial increase in short-circuit current density (J_{sc}) from 19.93 mA/cm^2 to 34.18 mA/cm^2 and fill factor (FF) to 87.68% more than compensated for this reduction. Consequently, the power conversion efficiency (PCE) increased significantly from 21.79% for the single-absorber reference structure to 40.88% for the optimized trilayer solar cell.

The findings of this chapter not only underscore the benefits of trilayer graded-bandgap architectures for lead-free perovskite solar cells but also provide a clear pathway for further development and experimental realization. These results confirm the effectiveness of the proposed multilayer design strategy and highlight the strong potential of lead-free perovskite materials (K_2LiAlI_6, $RbGeBr_3$, and $FA_4GeSbCl_{12}$) for the development of high-efficiency next-generation photovoltaic devices. The findings will serve as the foundation for future work aimed at bridging the gap between simulation and practical device fabrication.

References Chapter 3:

[1] Ayyaz, M., Ali, W., Ahmad, I., Khan, M. I., & Alharbi, H. F. (2025). Numerical investigation of lead-free double perovskite K_2LiAlI_6 solar cells using SCAPS-1D simulation.

[2] Lu, Y., Chen, X., Pan, G., Chen, Q., Chen, L., Wang, H., Wen, J., Peng, C., Li, C., & Wu, J. (2026). Numerical simulation and optimization of all inorganic $RbGeBr_3$ perovskite solar cells. Solar Energy, 303, 114119.

[3] Shukla, R. K., Srivastava, A., Wadhwani, N., Shukla, S., & Singh, N. (2025). Modeling and simulation of lead-free, formamidinium germanium-antimony halide ($FA_4GeSbCl_{12}$) based solar cell. Journal of Optics. https://doi.org/10.1007/s12596-025-02599-6

[4] Dar, S. A., & Sengar, B. S. (2024). Design and performance optimization of a novel tri-layer unleaded all inorganic lead-free mixed halide CsSnI3-x Brx heterojunction solar cell. Solar Energy, 275, 112618.

[5] Tinedert, I. E., Saadoune, A., & Hossain, M. K. (2024). A theoretical study of all-inorganic perovskite solar cells: computational modeling of the CsPbI3/RbGeI3 bilayer absorber structure. *Journal of Physics and Chemistry of Solids*, *189*, 111951.

[6] Siddique, M. A. B., Shahadath, N., Tarekuzzaman, M., Kabir, M. R., Ahmad, S., Khokan, R. M., ... & Hasan, M. Z. (2025). Performance evaluation of Eu 2 NiMnO 6-based lead-free perovskite solar cells: a SCAPS-1D study. RSC advances, 15(42), 35488-35508.

[7] Ali, M. E., Amanullah, M., & Mia, M. R. Strain-Dependent First-Principles Investigation of Na3OI Anti-Perovskite: Performance Evaluation with Various ETL Materials for Efficient Solar Cells. Available at SSRN 5437092.

[8] Mottakin, M., Sarkar, D. K., Selvanathan, V., Rashid, M. J., Sobayel, K., Hasan, A. M., ... & Akhtaruzzaman, M. (2023). Photoelectric performance of environmentally benign Cs2TiBr6-based perovskite solar cell using spinel NiCo2O4 as HTL. Optik, 272, 170232.

[9] Pindolia, G., Shinde, S., & Jha, P. K. (2023). P3CPenT as an organic hole transport layer for perovskite solar cells. International Journal of Quantum Chemistry, 123(18), e27149.

[10] Sarkar, D. K., Mottakin, M., Hasan, A. M., Selvanathan, V., Sobayel, K., Khan, M. N. I., ... & Akhtaruzzaman, M. (2023). A comprehensive study on RbGeI3 based inorganic perovskite solar cell using green synthesized CuCrO2 as hole conductor. Journal of Photochemistry and Photobiology A: Chemistry, 439, 114623.

[11] Khatoon, S., Chakraborty, V., Yadav, S. K., Diwakar, S., Singh, J., & Singh, R. B. (2023). Simulation study of CsPbIxBr1-x and MAPbI3 heterojunction solar cell using SCAPS-1D. Solar Energy, 254, 137-157.

General conclusion

General Conclusion

In this study, a comprehensive numerical investigation of lead-free perovskite solar cells was carried out using the SCAPS-1D simulation software, with the aim of improving photovoltaic performance through absorber-layer engineering and systematic device optimization. The study proposes a new device architecture based on emerging and innovative materials, namely K_2LiAlI_6, $RbGeBr_3$, and $FA_4GeSbCl_{12}$, which have not been extensively explored in the literature. The study began with the analysis of a reference single-layer solar cell based on the structure ITO/TiO_2/K_2LiAlI_6/CuI/Au, which achieved a power conversion efficiency of 21.79%, confirming the validity of the adopted simulation model through its close agreement with previously published results. To enhance solar spectrum utilization, a second absorber layer based on $RbGeBr_3$ was introduced, forming a bilayer structure (ITO/TiO_2/K_2LiAlI_6/$RbGeBr_3$/CuI/Au) that raised the efficiency to 33.51%. A further improvement was achieved by incorporating a third absorber layer, $FA_4GeSbCl_{12}$, resulting in a novel trilayer architecture (ITO/TiO_2/K_2LiAlI_6/$RbGeBr_3$/$FA_4GeSbCl_{12}$/CuI/Au) that reached an efficiency of 35.75%. Several hole transport layer (HTL) materials were examined, including CFTS, Cu_2O, $CuCrO_2$, CuI, CuO, NiO, Spiro-OMeTAD, P3CPenT, PEDOT:PSS, and CuSCN. Copper(I) iodide (CuI) was identified as the most suitable HTL owing to its favorable compatibility with the proposed structure, achieving a high fill factor of 86.74%. Moreover, systematic optimization of the absorber-layer thicknesses and acceptor concentrations was performed, yielding optimum values of 100 nm, 500 nm, and 800 nm for K_2LiAlI_6, $RbGeBr_3$, and $FA_4GeSbCl_{12}$, respectively, and 1×10^{17} cm^{-3}, 2×10^{13} cm^{-3}, and 1×10^{20} cm^{-3} for their corresponding acceptor concentrations. As a result, the optimized trilayer device achieved outstanding photovoltaic characteristics, including a power conversion efficiency of 40.88%, an open-circuit voltage of 1.37 V, a short-circuit current density of 34.18 mA/cm^2, and a fill factor of 87.62% under AM1.5G illumination at 300 K. It is worth noting that although the open-circuit voltage decreased progressively from 1.60 V for the single-layer device to 1.37 V for the optimized trilayer structure, the substantial increase in current density and fill factor more than compensated for this reduction, resulting in a net gain in overall efficiency.

Overall, the findings of this work demonstrate that the proposed novel architecture, based on new and emerging materials, significantly improves solar spectrum utilization, charge-carrier generation, and overall photovoltaic performance. These results highlight the strong potential of these innovative lead-free perovskite materials for the development of high-efficiency and

environmentally friendly next-generation perovskite solar cells. We hope that this study will inspire further research and innovation in the development of sustainable solar energy solutions and the realization of advanced photovoltaic devices.